R79-914346-4

Program to Investigate Advanced Laser Processing of Materials

E.M. Breinan
C.O. Brown
D.B. Snow

FIRST ANNUAL REPORT

Summary of Work Performed:
1 June 1978 — 31 July 1979

August 1979

Prepared under Contract N00014-78-C-0387

Sponsored by

Defense Advanced Research Projects Agency
ARPA Order No.3542

Prepared for

Office of Naval Research

UNITED TECHNOLOGIES RESEARCH CENTER

UNITED TECHNOLOGIES

EAST HARTFORD, CONNECTICUT 06108

(6) Program to Investigate Advanced Laser Processing of Materials.

UNITED TECHNOLOGIES CORPORATION
RESEARCH CENTER
East Hartford, Connecticut

(14) UTRC / R79-914346-4

(15) N00014-78-C-0387, new ARPA Order-3542

First Annual Report under Contract
Summary of Work Performed for the Period
(9) Annual rept. no. 1, 1 June 1978 to 31 July 1979;

(11) Aug 79

ARPA Order No:	3542
Program Code No.:	000008D10K71
Contractor:	United Technologies Research Center
Contract Date:	1 June 1978
Contract Amount:	$790,000
Contract No.	N00014-78-C-0387
Contract Expiration Date:	30 November 1980
Short Title of Work:	Laser Materials Processing
Principal Investigator:	(10) Dr. E. M. Breinan (203) 727-7396
Scientific Officer:	Dr. Bruce A. MacDonald
Reported by:	E. M. Breinan, C. O. Brown, D.B. Snow

(12) 93

Sponsored by Defense Advanced Research Projects Agency

409252

JOB

FOREWORD

This program has been conducted under the sponsorship of DARPA through Dr. Ed Van Reuth and has been monitored by Dr. Bruce MacDonald of ONR. A number of UTRC scientists who are not listed as authors have made significant contributions to the program as follows:

Dr. Bernard H. Kear has been a major consultant on this program, and has been responsible for the generation of many of the underlying concepts and the integration of these concepts with the major field of rapid solidification technology. Mr. Frank L. VerSnyder has provided high-level managerial guidance and his experience in setting priorities and goals on process development research has been responsible for the smooth progress of the program to date. Substantial advice and guidance in the fields of alloy design and solidification have been contributed by Dr. Earl R. Thompson, Dr. Frank D. Lemkey and Dr. David D. Pearson who have drawn heavily on their expertise in design of alloys for directional solidification in order to benefit this program. Dr. Brice N. Cassenti has done the stress calculations while Dr. Larry E. Greenwald has contributed in the area of thermal analysis and heat flow. Finally, Mr. Ruel Wicks and Mr. Herb Tourtellotte have been responsible for apparatus and equipment design and development.

TABLE OF CONTENTS (Cont'd)

Program to Investigate Advanced Laser Processing of Materials

TABLE OF CONTENTS

Report R79-914346-4

Program to Investigate Advanced Laser Processing of Materials

SUMMARY

During the course of the initial program year, UTRC's program to produce and spin test a 12.7 cm diameter turbine disk using the LAYERGLAZE™ Process fabrication technique has seen major milestones met in both the Processing and Alloy Design areas. Specifically, in the Processing area, a powder feed LAYERGLAZE apparatus has been designed, constructed, and used to produce LAYERGLAZE parts for mechanical test, and a 13.2 cm diameter, 3 cm thick scale model disk preform. Mechanical testing and microstructural analysis showed the LAYERGLAZED material to have excellent microstructure, along with good structural integrity and freedom from serious fabrication flaws. It thus appears that the process and the apparatus will be capable of producing test disks which will meet the program's major objective of a spin test in late 1980.

In the alloy design area, a technique for effective, rapid screening of alloys for LAYERGLAZE fabricability has been devised. Early experience showed that all but the weakest of conventional superalloys crack under LAYERGLAZE fabrication conditions. Therefore, the alloy development task assumed the challenging role of identifying strong ductile alloys which are also fabricable by the LAYERGLAZE process. To date, a preliminary series of alloys based on the Ni-Al-Mo system has been identified, and one composition, Ni-8Al-12Mo-3Ta (at %) has been LAYERGLAZE fabricated and mechanically tested. Although its strength is good in the as-fabricated condition, it does not reach the level of Gatorized IN-100, the most advanced material currently in use as turbine disks. Nonetheless, the relatively flaw-free nature of LAYERGLAZED 8-12-3 suggests that alloys of this type may be applied under a higher fraction of their strength than conventional alloys.

The 8-12-3 is not intended to be the final program disk alloy, but is simply the first promising member of a series to be evaluated during the next program year. 8-12-3 has also demonstrated a phase instability at the highest test temperature 704°C (1300°F), which causes loss of strength and axial ductility. Four additional compositions, all stronger than 8-12-3 and on the basis of initial results found to be more phase-stable at 1300°F, have been identified and shown to be potentially fabricable by LAYERGLAZE. These alloys constitute the major emphasis of our 1979-80 fiscal year program.

During the next program year, fabrication work will concentrate on improved structural uniformity and integrity. Specific improvements will be sought in the ability to control the uniformity of powder feed mass flow, powder handling under improved atmospheric conditions, and improved fabrication atmosphere to minimize the possibility of contamination. Fabricability tests and microstructural characterization will be conducted on the additional four candidate alloys, followed by mechanical test evaluation of all compositions which prove fabricable. From these test results, the best composition for disk fabrication will be chosen, and disk production will be begun.

The program is running well, with the probability for meeting the program goals rated as very good. Successful fabrication of the first full-size disk preform ahead of schedule has practically eliminated the possibility that residual stress buildup will be a serious problem, but has shown also, that our choice of alloys will definitely be limited. Observations to date have indicated other potential process advantages such as in-situ inspectability, and ability to grade stress, composition, and structure for future investigation.

The two main areas of question in the coming year's work involve the demonstration of fabricability of stronger alloys along with their high-temperature phase stability, and our ability to consistently produce large volumes of essentially flaw-free material by a small-increment buildup process. Preliminary indications in both areas are positive, and, relative to the question of ability to control defects in fabrication, the process on a quantitative scale does not appear to be as difficult to control as was originally anticipated. The coming year's research should see many of the remaining questions answered.

INTRODUCTION AND BACKGROUND

The research described in this report was initiated in August 1978. Initially, scientists at United Technologies Research Center invented the LASER-GLAZE Process for production and control of rapidly chilled metallurgical microstructures in late 1975. This process and associated scientific research in the area of Laser Melting and Rapid Solidification are described in Refs. 1-12.

Primarily, the basic idea of rapid solidification processing is to produce homogeneous or uniform metallurgical microstructures. Given the fact that materials ultimately fail as a result of inhomogeneities in the structure, improvement in homogeneity will allow utilization of a larger fraction of the ideal material strength; that is, improved material performance capability. Homogeneity is normally at its greatest in the liquid state. Upon normal solidification and subsequent slow cooling in the solid state, phase separation and segregation occur. Once inhomogeneities are created in the solid, it is difficult to rehomogenize the material without remelting it. Although various materials processing operations will improve the homogeneity while still in the solid state, they will not usually be capable of producing optimal structures once the material has segregated.

Rapid solidification processing makes use of the high degree of liquid phase homogeneity. By sufficiently rapid solidification and subsequent rapid cooling through the highest temperature regions in the solid state, uniform structures with a high degree of homogeneity can be maintained to sufficiently low temperatures that they become stable. These structures can often be generated by controlling the solidification and cooling rates, and desirable structures tailored to performance requirements can be selected. By using rapid solidification techniques to select and control material structures, the technology promises to raise material performance levels in the future.

Laser melting, while just one of several techniques for rapid solidification processing, appears to offer numerous advantages, the most prominent of which is in-situ consolidation. Although rapid solidification still must be accomplished in thin sections, when fabricated by laser, the sections are consolidated together as they are added, obviating the need for further consolidation or exposure to elevated temperature. This is the main difference from the "powder metallurgy" or "ribbon" approaches to rapid solidification, and may ultimately be significant in the technology.

The LASERGLAZE Process was rapidly recognized as having obvious potential for treatment of metal and alloy surfaces and alteration of properties through structural selection and control. Material property areas where surfaces are important include erosion resistance, wear resistance, corrosion resistance, and, to the extent that fatigue crack initiation occurs at surfaces, fatigue resistance. Analysis of the heat flow considerations involved with LASERGLAZE revealed that, as with any other rapid solidification and quenching technique, high cooling rates could be achieved only in thin sections, with the maximum cooling rates increasing as the section thickness decreased. Figures 3 and 4 of Ref. 4 summarize these heat flow calculations. The conclusion was that the effects of LASERGLAZE on material properties were limited to what could be accomplished by structural modification and control of thin surface layers. This restriction was considered to be the most severe limitation of the new technology.

A logical, though not immediately obvious extension of the LASERGLAZE technology was the concept of sequential deposition of rapidly solidified and cooled thin layers to build up a bulk, rapidly-solidified material with a homogeneous, controlled microstructure. The evolution of this concept, eventually termed the LAYERGLAZE Process made possible for the first time the fabrication of bulk, rapidly solidified materials which, in contrast to the powder metallurgical approach, could be fabricated to full density without the need for a post-fabrication consolidation or densification step.

The initial LAYERGLAZE concept was evaluated under DARPA sponsorship between March and September 1977, and the results of this Performance and Cost Benefit Analysis are reported in detail in Ref. 13. This program was conducted to assess the potential performance and cost benefits which could be realized if the LAYERGLAZE Process could be developed to fabricate gas turbine engine disks, and also to establish and demonstrate the technical feasibility of the physical process for LAYERGLAZE buildup. The results and conclusions of this preliminary evaluation are summarized below.

A. Major Conclusions

1. Performance

A 50% reduction in the live (load carrying profile) disk weights of the JT10D-4 can be realized for the high pressure compressor, high pressure turbine and low pressure turbine rotors, when designed using LAYERGLAZED alloys with assumed properties. This amounts to a minimum of 400 lbs (181.8 kg)/engine.

2. Cost

The total estimated Life Cycle Cost (LCC) reduction due to the use of LAYERGLAZED alloys in the F-100(3) engine for the F-15 aircraft, when designed for optimum LCC in the high pressure compressor and maximum weight savings in the remaining components, is $222.4 million.

3. Process Feasibility

The LAYERGLAZE process for sequential, in-situ buildup of dense, high cooling rate structures appears to be feasible at rates of 0.5 cu in/min (8.2 cc/min) at the 6.0 kW laser power level, with deposition rates of 1.0 cu in/min (16.4 cc/min) anticipated in the 10.0-15.0 kW power range. Thermal calculations indicate that the part can be cooled and rapid cooling rates can be maintained in large parts.

4. Alloy Design Concept

High yield strength alloys were produced from eutectic starting materials; the results from the NiMoAl alloy which displayed a yield strength of 1755 MPa at 760^{o}C suggest a fruitful path for further alloy optimization.

B. Additional Results and Conclusions

Task 1 - Performance and Cost Benefits/F-100(3)

1.1 Design evaluations of the F-100(3) and FEAT engines indicated that yield strength was less important than LCF and fracture toughness, pointing the way for emphasis in the areas of microstructural perfection and in-situ inspectability during future process development work.

1.2 A composite engine layout depicting the present B/M F-100(3) as compared to the redesigned engine using LAYERGLAZE processing was shown.

1.3 The total expected weight savings from using LAYERGLAZE processed PDS alloys in the F-100(3) is 111.3 lbs (51.4 kg).

1.4 A manufacturing cost reduction of $27,900/unit (17% of cost of parts studied) is projected for the F-100(3) engine by using LAYERGLAZE processed PDS alloys.

Task 2 - Performance and Cost Benefits/FEAT

2.1 A composite engine layout depicting the present B/M FEAT as compared to the redesigned engine using LAYERGLAZE Processing was shown.

2.2 The total expected weight savings from using LAYERGLAZE processed PDS alloys in the FEAT is 71.8 lbs (32.6 kg).

2.3 A manufacturing cost reduction of $9,600/unit (16% of cost of parts studied) is projected for the FEAT engine by using LAYERGLAZE processed PDS alloys.

Task 3 - Performance and Cost Benefits/JT10D-4

3.1 Although strengths of 200,000 psi (1380 MPa) and 300,000 psi (2070 MPa) were assumed for Ti and Ni base alloys respectively, substantial fractions of the total predicted weight savings can still be realized at much lower strength levels, i.e. ~80% of weight savings could be realized with alloy strengths as much as 30% below those sought.

3.2 Total weight savings for the engine parts analyzed is predicted to be no less than 400 lbs (181.8 kg) which is equivalent to a reduction of 0.40% in Direct Operating Cost + Interest. By optimizing the way in which improved material properties are utilized, weight savings could potentially be increased by approximately 100 additional pounds (45.4 kg) (equivalent to 0.478% DOC + INT).

3.3 Because the rotor weights can be reduced with LAYERGLAZE process it is possible to also save weight at the bearing supports. Maneuver loads will be reduced due to smaller rotor weight thus possibly reducing case thicknesses. However, where static structures are limited for deflection requirements, no weight savings would be realized.

3.4 Cases fabricated by the LAYERGLAZE process could result in some weight savings where the design is limited by containment or LCF. Wall thickness could be reduced with a high ultimate and fatigue strength material.

3.5 Manufacturing cost estimates indicated that there would be no predictable difference in the manufacturing costs for commercial engines with LAYERGLAZED parts, so that predicted performance/weight/DOC+INT gains would be obtained without initial cost increases.

Task 4 - Life Cycle Cost Studies/F-100(3), FEAT

4.1 Maximum impact on life cycle cost savings was not coincident with maximum weight reduction in all cases. Extension of part life to the cycle limit, and acquisition cost reduction are the most potent factors.

4.2 According to design personnel, the ability to tailor structures for added life with LAYERGLAZE processing is potentially the most important benefit of the technology. The flexibility to adjust the structure, and to opt for specific properties is not available to the same degree in presently utilized materials systems.

4.3 The total estimated Life Cycle Cost reduction due to the use of LAYERGLAZE/PDS alloys for the F-100(3) engine in the F-15 aircraft, when redesigned for maximum weight savings, is $141.7 million. When optimized from the LCC standpoint, rather than weight savings, the total estimated Life Cycle Cost reduction was $222.4 million.

4.4 The total estimated Life Cycle reduction due to use of LAYERGLAZE/PDS alloys for the FEAT engine in the ATS aircraft due to initial cost and weight reduction is $103.4 million. (Since the FEAT is designed based on presently unobtainable advanced material properties, should its construction be made possible by LAYERGLAZE technology, this technology should "get credit" for the much larger performance and cost benefits inherent in the FEAT design.)

Task 6 - Technical Feasibility Demonstration

6.1 Cooling rates of 10^5-10^6°C/sec can be produced at power densities in the range of 10^4-10^5 watts/sq cm, a level comfortably within the equipment capability. (It has been shown under Task 7 that alloys produced at these cooling rates have exhibited significant properties.)

6.2 Process efficiency increases with increased cooling rate, with less specific energy being required for unit deposition of new material. Increased power densities and higher processing speeds (shorter dwell times) are required to obtain higher cooling rates.

6.3 Thermal analysis modeling the LAYERGLAZING process indicated that a 1 in. wide, 0.001 in. strip on the surface of a disk could achieve a cooling rate in excess of 10^6°C/sec.

6.4 Observations of the deposition process to date indicate that substantial progress in LAYERGLAZE processing will result from further development effort.

6.5 A 0.200 in. (0.508 cm) deep flange of type 304 stainless steel was fabricated using a small scale LAYERGLAZE apparatus which applied material by a wire feed technique. Flange material was fully dense and free of flaws as inspected by radiography.

Task 7 - Alloy Design and Evaluation

7.1 In order to obtain high strength coupled with ductility, the best approach appears to be through the preparation of metastable, single phase alloys which are hardened by phase decomposition in the solid state.

The potential of the LAYERGLAZE Process having thus been established, the present program was proposed, eventually procured, and was begun officially in August 1978. This program for Fabrication and Testing of a Scale Model LAYERGLAZE Turbine Disk involves six tasks, including:

Task 1 - Definition of a suitable method of LAYERGLAZE disk fabrication for a 5 in. (12.7 cm) diameter test part.

Task 2 - Identification of an alloy suitable for LAYERGLAZE model disk fabrication and testing.

Task 3 - Design and construction of the apparatus necessary to fabricate a 5 in. (12.7 cm) diameter test part.

Task 4 - Design of a suitable model disk part and a suitable spin test.

Task 5 - Fabrication and test of one 5 in. (12.7 cm) diameter model turbine disk, according to results of Task 4.

Task 6 - Fabrication of additional demonstration disks within the scope of available funding.

This program has been underway for the past year and, to date, is running on or ahead of schedule in all tasks and milestones. The following text reports in detail the results of this first year's effort.

EXPERIMENTAL PROCESSING OF LAYERGLAZED MATERIALS

A. Apparatus

The LAYERGLAZE Process requires the use of a high power optical beam at a power density of between 0.15-1 x 10^5 watts per square centimeter. As a consequence, an environmental control chamber must be used so that an acceptable shield gas such as He can be controlled around the interaction region. Introduction of the gas provides protection for the interaction region and prevents optical breakdown from occurring. This chamber, along with other essential components to the process, is shown in Fig. 1. The optical beam from the laser is first turned by an optical flat mirror, M_1, and redirected to the focusing mirror, M_2. The focusing beam is then transmitted into the environmental chamber through a small diameter aperture. Interaction with the workpiece takes place approximately 5 cm below the aperture. The wire feed nozzle is attached to the chamber and directs the wire in space to the interaction region on the arbor. A different nozzle in the same position is substituted when powder is fed to the interaction zone. The arbor, which in all cases was a 304 stainless steel cylinder 5 cm long by 3.7 cm diameter with a 3.2 mm wall thickness, is water cooled through a specially fabricated mandrel. This mandrel is attached to a variable speed motor in order to vary the rotational speed. The complete assembly is attached to an X,Y,Z table which allows for full motion of the arbor to allow for the LAYERGLAZE buildup.

Figure 2 shows a larger environmental chamber fabricated under a UTRC program and used in conjunction with a numerical controlled vertical miller. The numerical-controlled system is capable of linear speeds up to 7.62 cm/sec and has linear interpolation so that motion is essentially uniform in all planes. With this new system, it is possible to completely automate the LAYERGLAZE Process.

The wire feed system is shown in both Figs. 1 and 2 and is a commercially available dual-drive unit capable of delivering wire from a fraction of a centimeter per minute to over 100 centimeters per minute. Wire size can be varied between 0.051 to 0.127 cm diameter.

When powder is being used as the working fluid, the wire feed system is replaced with a powder feed system, see Fig. 2. A vibrator is used to provide mechanical shaking which starts the gravity powder flow process. Figure 3 shows the stream of powder being emitted from the nozzle under typical run conditions. It should be noted that the nozzle-to-workpiece distance is typically 6.3 mm (1/4 in.) for both the wire and powder. Within this range, the powder stream approximates a straight line.

B. Determination of Process Criticality

The initial phase of this program was devoted to determining the critical parameters which are required to achieve a uniform homogeneous, nonporous, LAYERGLAZED part. The data and the LAYERGLAZED parts reported in the final report, Assessment of Advanced Laser Materials Processing Technology (Ref. 13), were achieved with an optical system that generated a Gaussian-shaped beam. Table I gives the typical operating conditions used to obtain this information. Data taken from a high speed movie taken of the process were used to generate some of the numbers listed, column 1. In the present program, the laser system was changed because it was felt that a Gaussian beam was not necessary for the process and at UTRC a crossflow laser was available with a suitable, high quality unstable resonator beam. As such, the parameters were then adjusted to give an approximately equal power per unit area, column 2. A comparison of the results showed that even though the prior reported results were at best only poor to good in comparison, the new results could only be judged as poor. Examination of the results at this time indicated that one possible problem could be explained by high-power densities which caused optical breakdown and spiking in the fusion zones that were being produced. The result was to decrease the power density by decreasing the power and by increasing the laser beam spot size. Once this was achieved, column 3, the optical breakdown problem seemed to have disappeared.

With the breakdown problem under control, the process of achieving uniform deposition of the 308 stainless steel wire on the stainless steel mandrel was faced. Figure 4 shows a problem of droplet transfer that was encountered. This drop transfer was detrimental to the process, because large droplets, as shown in Fig. 4a, were transferring to the arbor in a periodic fashion. It was noticed early that the drop transfer was neither consistent in size nor in its periodicity and that under certain conditions, the drop transfer was nearly nonexistent and that the material transfer was very smooth. Many samples were produced under varied experimental parameters until the most optimum condition was achieved. Figure 4b shows such a condition. Figure 4c shows the effect of drop transfers after several layers of buildup. Once the pattern is set on the first pass, as the process goes over the perturbation represented by an already transferred droplet, the droplet acts as a "rake" and removes all of the molten pool from the wire causing the perturbation to grow. This, of course, was unacceptable.

The final near-optimum relationship between the optical beam, the arbor, and the wire are depicted in the isometric drawing of Fig. 5. With the arbor rotating in a counter-clockwise direction at a rotational speed of ω, a teardrop shaped molten zone is obtained on the arbor at steady state when the impinging optical beam is circular, as shown. The teardrop is typically twice as long as the beam diameter. The spatial location of the wire is at this point, probably the most critical of all parameters. The angle of the wire

relative to the plane at the interaction point was held to 30^{o} and the extended length of the wire beyond the nozzle tip was held to 6.3 mm (1/4 in.). If the wire extension is longer, it cannot be precisely located at its tip, and if it is too short, the nozzle interferes in the interaction zone. It was found that the wire had to touch just in front of the molten pool, as shown, in order to give proper material transfer. If the wire wanders from one side to the other, it would be split by the laser resulting in incomplete melting. If the wire is displaced in the plane of rotation then conditions could allow drop transfer or wire instabilities, Fig. 6. If the wire is allowed to pass over the beam and touch inside the molten pool area, then melting of the wire occurs at some height above the arbor, allowing a large droplet to form until it drops onto the surface because of its weight. Likewise, an unstable condition is also achieved if the wire is allowed to touch the arbor $\geq$2 wire diameters in front of the molten pool. In this case, the wire becomes too long and moves around randomly causing instabilities. The only stable condition is shown in the figure with a displacement of the wire of up to 2 wire diameters allowed for stability. It should also be noted that the interaction zone is substantially below the focal plane as indicated in Fig. 6. The photographs of Fig. 7 show what effect power distribution has on the shape of the fusion zone. In this case, a 60.96 cm focal length mirror was used. The beam from this mirror impinged upon the test sample that was set up as an inclined plane. Thus, the fusion profiles above and below the focal plane could be determined. At the focal plane, using a 6 kW optical beam, the power density is approximately 0.418×10^{6} w/cm^{2}, whereas at 64.8 cm, the power density is $\sim 0.78 \times 10^{5}$ w/cm^{2}. The graph of Fig. 8 depicts in another way how the beam diameter varies as a function of position. As the number of test specimens increased it was determined experimentally that a power density of approximately 0.78×10^{5} watts/cm^{2} gave the best appearing deposition.

C. Wire Feed Development

The initial stages of the program were devoted to determining what parameters were required to deposit stainless steel wire on a stainless steel arbor. The decision to use this procedure was based on the philosophy of allowing model tests to be run in such a way that the process itself could be understood without being complicated by materials effects. The wire feed system was described previously along with the experimental procedure required to deposit material on the arbor. In all cases, the wire diameter was 0.089 cm. These tests were designed to allow for smooth deposition of wire on the arbor. Once the proper parameters were obtained tests were initiated to determine the requirements for deposition of multiple-layers of wire on an arbor.

The first parameter changed was the cross-feed rate which in turn would determine what, if any, was the effect of laying the wire adjacent to or overlapping the previous pass. Figure 9 shows a closing up of the single pass spiral as the cross-feed rate is decreased from 0.085 cm/sec down to 0.051 cm/sec, the lower limit of the x-y table. A similar series of tests, Fig. 10, was then run with 5 layers of wire being LAYERGLAZED onto the arbor to determine what if any effect the overlay had on the process and how it affected the metallurgy of the sample. The macroetched cross sections for the five layer cases are also shown in Fig. 10 and it is obvious that the slower cross-feeds result in superior deposition both in uniformity of the matrix and of the surface. Thus a cross-feed rate of 0.051 cm/sec was chosen for the remainder of the tests.

The test was then extended to determine whether or not any problems would be encountered with a very large number of layers deposited. An arbor was prepared with a total of 58 layers. A direct comparison of the surface condition for 1, 5 and 58 layers is seen in Fig. 11. As the number of layers is increased the surface becomes substantially rougher. The cause for this occurrence is most probably the enhancement of small imperfections or instabilities deposited at the earlier stages.

The 58 layer sample was then subjected to several tests. The first one was the machining of the outer surface to see if any imperfections could be found below the rough surface. A direct comparison between the as-deposited state and the machined surface is seen in Fig. 12. The machined surface was determined to be quite smooth with only a few minor imperfections being uncovered.

The sample was then cut along the axis on one side with a 0.330 cm width cutting wheel. When the cut was completed, the arbor sprung open 0.190 cm. This was considerably less than half of the normal springback for the mandrel tube, indicating that very high compressive forces on the arbor were present as a result of the deposited material in the process. (See Appendix A). A wedge along the length of the arbor was then removed so that the sample could be examined metallurgically. Three different macroetched photographs of the 58 layer deposit, Fig. 13, show the quality of the structure. The upper surface in Fig. 13a is the surface that was machined. The lower surface is the 304 stainless steel arbor. Two major concerns can be noted when examining the macrophotograph, Fig. 13a. One is the deep penetration type spiking that occurs throughout the deposit and the other is the voids associated with the spiking. These are shown more clearly in Figs. 13b and 13c. The deep penetration spikes were unexpected because it is known that deep penetration occurs at power densities in the range in excess of 10^6 w/cm^2. The conditions under which this sample were generated, involved a power density of only 0.62×10^5 w/cm^2, far below that normally required for deep penetration. A melt cross section obtained

under similar conditions is shown in Fig. 7 at 64.8 cm and there is an obvious lack of deep penetration. Several possible causes of the spikes were examined and the only plausible one deals with the rough surface of the arbor which is present after the wire is deposited. The rough surface is formed when two adjacent passes that overlap are deposited onto the arbor, Fig. 9. The high freezing rates associated with the process along with surface tension forces combine so as not to allow the material to flow into a flat, uniform surface. As a consequence, a well or "v" groove is formed on the surface of the first and subsequent layers. As the process is reversed and the wire is deposited with an opposite spiral, a cavity is formed at the intersection of the top layer and the layer on which it is deposited. This cavity becomes a steep-walled radiation trap for the 10.6μ radiation. Under these conditions it is very reasonable to expect that the power density at the base of the cavity could exceed 10^6 w/cm^2, thus causing the deep penetration type spiking and the associated voids. The voids are normally formed at the root of the spike because of the rapid solidification rates that the materials experience at this location.

D. Powder Feed Development

The program was reevaluated following initial wire-feed studies, and different options were considered in an effort to alleviate the problems of the deep penetration type spiking that were associated with the wire feed. Two primary options included either the reduction of wire size or the use of powder in order to reduce the scale of surface irregularities. Both of these options initially presented problems because smaller wire diameters were difficult both to obtain and to handle, while severe difficulties had been associated with all previous attempts to feed powder directly into the laser beam. Some preliminary tests with a simplified powder-feed setup (see Fig. 3), however, indicated that there was a possibility that the process could be made viable, and, based on the first deposits made during preliminary tests, decisions were made to develop a powder process and to convert a representative alloy ("8-12-3" was chosen, see alloy design section) into powder for fabrication tests. The primary motivation for this decision was that obtaining LAYERGLAZE alloy powders was far easier and faster than obtaining the same alloys in wire form. If the powder could be made to work, it would facilitate rapid progress to the point of being able to obtain mechanical test data on actual LAYERGLAZE-fabricated material.

A powder delivery mechanism was fabricated employing the simple technique described above. The powder delivery rate from the 8-12-3 mixture was experimentally determined to be 0.14 gm/sec, Fig. 14. One problem encountered with the powder feed was the inability to deliver constant mass flows for long periods of time. Using a 0.089 cm diameter nozzle, the range of mesh sizes was found to be most critical. The optimum powder size was found to be from -170 mesh to +500 mesh. If only finer powder size fractions were used the

powder feeder would clog. Conversely, if the large powder sizes were used free flow would be achieved, but the powder flow rate could not adequately be controlled. It should be noted that use of as wide a range of mesh sizes as possible was desirable because of the yield factor.

Upon the receipt of the 8-12-3 powder a series of tests was designed to determine what operating parameters would yield the best deposits. The first of these was the criticality of alignment in the interaction zone between the optical beam, the arbor, and the powder. It was found that the criticality of this parameter was identical to that determined for wire feed with the arrangement being the same as depicted in Figs. 5 and 6. The location of the stable region was about the same. In the unstable region, the appearance of the surface changed appreciably from that of the wire deposition. The powder when injected into the beam volume would melt and spatter. Also, it caused optical breakdown because the beam was being seeded with the powder. When operating in the stable region the surface of the deposited material was very smooth, Fig. 15. For the samples shown in Fig. 15 approximately 1/3 cm of the 8-12-3 powder was LAYERGLAZED on the standard water-cooled, stainless steel arbor. The deposit was made almost 2.5 cms wide so that end effects could be distinguished from the bulk of the deposited material. From the onset of the powder tests, it was obvious that, under optimum conditions, both the ease of deposition and quality of the deposit were potentially superior to those characteristic of wire deposition. This was evident just by looking at the surface appearance. Figure 15 contains a comparison of the surface in the as-deposited condition and after reglazing. The glazed portion was achieved by turning off the powder feed and allowing the laser to remelt and smooth out the surface. The small spherical type "spatter" deposits located on the as-deposited section are remelted into the deposit on the glaze pass leaving an almost mirror smooth surface. A major additional advantage of the powder feed over the wire feed is that the laser coupling efficiency is much higher with the powder, leading to a much higher energy deposition efficiency, and, as a result of the facilitated coupling, enhanced process stability is achieved in the interaction zone.

It was felt that the quality of the deposit was also affected by such items as the optical power and the mass flow rate. A test was then run with the optical power at 3 kW, 4 kW, and 5 kW, Fig. 16. Obviously the 3 kW test did not allow for complete melting and flowing of the deposited powder, whereas at 5 kW complete melting and flowing did occur. This would be expected if the total energy and power density were allowed to decrease which it did. The 4 kW test was almost as good as the 5 kW test, however, there was evidence of slightly more spatter.

The mass flow rate of the 8-12-3 powder was increased by increasing the diameter of the nozzle from 0.089 cm to 0.114 cm. This is an increase in cross sectional area of 65 percent. If the flow rate increase is in direct proportion to the area, it would be expected that the mass flow would be increased by 65 percent. This in fact did not happen (Fig. 17) because the deposit per layer increased from 0.025 cm to 0.081 cm with the larger nozzle area. This is most likely due to the change in the friction or flow coefficient of the nozzle. Obviously from the difference in surface condition, Fig. 17, the slower flow rates are desirable with this energy input. The effect of increasing the mass flow is equivalent to a decrease in the energy per unit volume. The result is a very rough surface deposit which is not desirable.

E. Fabrication of Samples for Mechanical Test

Successful glazing of thin section deposits from the 8-12-3 powder was followed by attempts to build up heavy sections for mechanical testing of the alloy on the 3.8 cm diameter arbor. The acquisition of the numerical controlled vertical miller (Fig. 2) led to the simplification of the process. The computer was taped to control both the horizontal and vertical motion of the arbor while the LAYERGLAZE process was taking place. The data used to generate the tape came from experience in the deposition of the powder. It was found that under optimum conditions on the average 0.010 cm of material was added to the arbor on each layer.

The first glazed powder test sample (#1-8) generated using the new system is shown in Fig. 18. The overall diameter of the test sample was 6.45 cm. The initial surface speed was 8.47 cm/sec and the final speed was 14.2 cm/sec. This varied because of the outside diameter buildup with a constant rotational speed. The top surface is quite smooth except for a minor rounding off at the edges. This rounding off is due to the roll off of the powder at the edge. Along each side of the arbor, rough and porous spatter deposits are seen. This is due to powder loss over the edges into a region of low power density or low energy density where it is only partially fused to the substrate. Cleanup of the side surfaces was achieved by machining away these surface deposits, as shown in Fig. 19, and it should be noted that no pores or other imperfections were observed on either surface.

Metallurgical examination of sample 1-8 was very encouraging. Initially, the sample was cut in half, with the intention of sacrificing one-half for mechanical test specimens and saving the other half for display, or to use for additional test specimens as needed. The eventual sectioning and testing of sample 1-8 is described later, and detailed in Figs. 25 and 26.

The sample, as cut in half and macroetched, is shown in Fig. 20. The integrity of the deposited material, as well as the uniform layered structure, are obvious in this transverse section. It can also be seen that there is considerable compression on the central mandrel from the way it is deformed.

In Fig. 21, an end-view of the sample is shown. Of interest here is the strong tendency for epitaxial growth from layer to layer, resulting in what is essentially a radially directionally-solidified, layered growth pattern.

Structural analysis and mechanical testing of sample 1-8, as discussed in the following section, revealed that the material was sound, free of major flaws, had good structural integrity, reasonable strength, and excellent ductility.

F. Fabrication of Full Size Disk Preform

One additional fabrication task was performed during this reporting period. Based on the satisfactory characteristics of sample 1-8, a full size 13.2 cm diameter turbine disk preform was made as a fabrication exercise, primarily to demonstrate that a part of the full size could be made without encountering unforeseen problems such as excessive stress buildup during fabrication of larger diameters. This part is shown in the as-fabricated condition in Fig. 22, and machined to a typical turbine disk shape in Fig. 23. Its thickness varied from 3.2 cm adjacent to the mandrel to 2.3 cm at the outer diameter. The part was fabricated on a standard, 3.8 cm diameter, water-cooled stainless steel mandrel. Although initial intent was to fabricate the part from our alloy 8-12-3, which at the time of fabrication was our first program-generated disk alloy, we did not have a sufficient supply of 8-12-3 powder to complete the fabrication of a full-size part. The part was thus initially fabricated out to a diameter of 8.4 cm from the 8-12-3 alloy. To complete the fabrication, IN-718 alloy was used, as it was believed that this would serve to generate a full size part and thus allow us to demonstrate the feasibility of full size fabrication. Also, the change of material would demonstrate ability to alter composition. Since our experience with conventional superalloys had not shown any to be suitable for LAYERGLAZE fabrication, there was some question as to the fabricability of IN-718 by this process.

Fabrication was completed with both materials appearing to fabricate satisfactorily. A problem was encountered with curving of the outer surface, which in this test was solved with manual buildup, but which will require some future processing improvements for optimum disk fabrication.

Upon machining, although both alloys machined to smooth surfaces and appeared to have good structural integrity, some important differences in behavior were noted. Firstly, the 8-12-3 was much harder to machine, but produced a better surface finish. Only by using a finish grinding operation was it possible to fully smooth out the IN-718, indicating the possible presence of fine cracking. The final machined part in Fig. 23 is also shown with part of the surface macroetched, revealing the radial growth structure.

Eventually, this sample disk was cross sectioned, and is shown in Fig. 24. It should be noted that only one face had been machined, so that the sample possessed both an as-fabricated and as-machined face. As expected, the structure and the structural integrity of the 8-12-3 deposit was excellent. The IN-718, however, showed a type of microcracking in the plane of the disk which we call axial or Type II cracking. This observation is not considered as problematic in this program because alloy IN-718 is not intended to be a part of the program. The observed microcracking confirms our belief that few, if any, conventional superalloys can be satisfactorily fabricated by the LAYERGLAZE process. The program-developed alloy, 8-12-3, however, has proved to be adequately fabricable, and, it is noted in the alloy design section that there are several additional program-developed alloys which appear fabricable by LAYERGLAZE and possess improved properties.

The cross section in Fig. 24 shows that the compressive deformation in the inner mandrel is no greater than in the smaller diameter buildup in part #1-8. This confirms our calculations that compressive stress is maximized and that, eventually, the LAYERGLAZED material begins to support the material added above it. The ability to generate a compressive stress at the bore of the disk may eventually be exploited to the advantage of this type of fabrication. Appendix A is a summary of stress analysis calculations conducted under this program.

The total fabrication experience to date has indicated that a powder fed LAYERGLAZE system of the type described above is capable of fabricating parts of the size necessary to meet program goals, with good structural integrity.

ALLOY DEVELOPMENT FOR LAYERGLAZE FABRICATION

A. Introductory Comments

The development of nickel base superalloys for use as turbine components fabricated by the LAYERGLAZE Process was dictated by three sets of requirements; crack-free laser weldability, beneficial alloy response to rapid solidification ($>10^4$ $^oC/s$), and general properties exceeding those of current jet engine disks. To fulfill these criteria, both conventional and experimental alloys were evaluated. The primary consideration in examining any alloy was that it should remain crack-free after bead-on-plate deep penetration welding with a continuous, carbon-dioxide laser. Very few conventional nickel base superalloys of adequate strength, including those known to be weldable by other techniques, were able to pass this initial test. However, in the case of experimental alloy compositions, several alloys based on the nickel-aluminum-molybdenum system have proved to possess very encouraging properties, as will be described subsequently.

1. Laser Weld Cracking Evaluation

All alloys chosen for evaluation were first tested for resistance to laser-weld cracking. The selected alloys were made up from elements of ≥99.99% purity, melted together under argon in alumina crucibles, and chill cast into 0.8 x 5.7 x 17.8 cm slabs. Square blanks of approximately 0.8 x 2.8 x 2.8 cm size were cut from these slabs, ground smooth with a random scratch pattern on one face with 240-grit silicon carbide paper, and cleaned in acetone. These as-cast specimens were bead-on-plate deep penetration laser welded, ground face uppermost, with a continuous, carbon dioxide laser operated in the unstable resonator mode. As many as 16 specimens at one time were mounted near the rim of a 45.7 cm diameter, horizontal, rotating wheel - similar to that previously utilized for the LASERGLAZE Process (Refs. 11,14). The upper surface of each specimen was positioned so as to lie in the focal plane of the 45.8 cm focusing mirror. The wheel was rotated beneath the fixed point of beam impingement so that the effective beam traverse speed was 5.08 cm/s. The laser was operated at a power setting of 6 kW, so that the beam power delivered after window and mirror interface losses was ~4.7 kW, or ~1.0 MW/cm^2 beam intensity at the specimen surface. Most of the upper surface of each specimen was converted to a continuous layer of bead-on-plate welds with overlapping fusion zones by translating the rotating wheel on which they were mounted sideways by 0.38-0.76 mm per revolution. The specimens were shielded from oxidation during welding by covering the wheel with an aluminum shield and introducing a dynamic protective atmosphere of 100% helium flowing at 1.4 m^3/hr.

The entire welded surface of each specimen was examined for cracks at 30X with a stereoscopic microscope. In addition, its post-weld microstructure was observed on a plane cut perpendicular to the welded surface and to the welding direction. If no cracks were observed in the fusion zone or in the surrounding unwelded metal by either technique, the alloy was selected for further evaluation.

The transverse section through the overlapping fusion zones of each specimen was also used to measure the microhardness of each alloy, and thus to estimate its as-welded room-temperature strength. As-welded microhardness was found not to be dependent upon distance from the fusion zone free surface. Consequently, a standard procedure was adopted whereby 10 Vickers microhardness indentations were made with a 200 gram load on a transverse section at approximately one-half the depth of fusion zone penetration. Metallographic observations were made on this same transverse section to determine fusion zone profiles and depth, dendrite spacing, microporosity and/or microfissuring, if any. Some as-chill cast and as-laser welded specimens were examined by transmission electron microscopy (TEM) with a JEOL JEM-120 operated at 120 kV.

2. Differential Thermal Analyses

The phase transformation temperatures of most of the experimental alloys were determined by differential thermal analysis (DTA). Pure nickel was used as the standard in all cases. Both the heating and cooling rates were held constant at $5^{\circ}C$/min. Data from each specimen was recorded for at least two thermal cycles. In some cases the precipitation or dissolution of Ni_3Mo could not be detected by DTA. In this case, apparatus designed and built at UTRC was used to attempt to determine this particular phase transformation temperature by differential thermal expansion (DTE), again using a pure nickel standard.

3. Atomization

Some experimental alloys based on the nickel-aluminum-molybdenum system which exhibited crack-free laser weldability and relatively high as-welded microhardness were made up from pure metals and cast into single 22.7 kg ingots. These were converted to powder by the standard commercial argon atomization process by Homogeneous Metals, Inc. They were delivered to UTRC, packed in argon and sieved to -90 mesh. Each lot of alloy powder was then sieved further into specific powder size ranges to improve its flow characteristics.

4. Evaluation of Specimens Fabricated by the LAYERGLAZE Process

Specimens fabricated from laser-melted powder by the LAYERGLAZE Process were characterized by light microscopy, TEM, DTA, DTE, microhardness measurements and tensile testing. Most of this effort was directed toward disk 1-8. Half of this annular disk was sectioned into parallel-sided pieces, five of

which were ~3.6 mm (0.14 in.) thick and four of which were ~6.4 mm (0.25 in.) thick (Fig. 25). These were examined for porosity by radiography, then cut and ground into small tensile specimens (Fig. 26). The tensile specimens were oriented so that the load axis of each was parallel to either the disk radius (solidification direction) or perpendicular to it (disk rotational axis).

5. Identification Coding of Experimental Alloys

Experimental nickel base superalloy compositions which were developed in the course of this program were identified by a numerical code derived from the quantity of their elemental constituents in atomic percent. The number sequence of the code corresponds to the elements Al, Mo, Ta, Ti, Cr, and Hf, in that order. Thus, the alloy identified as alloy 8-12-3 had the composition 8 a/o Al, 12 a/o Mo, 3 a/o Ta, balance Ni. Alloy 11-12-0-0-5 was composed of 11 a/o Al, 12 a/o Mo, 5 a/o Cr, balance Ni.

RESULTS AND DISCUSSION

A. Laser Weld Cracking Evaluation

The initial selection of alloys for laser weld cracking evaluation was dictated in part by the usual factors thought to control weld-associated cracking in nickel base superalloys (Refs. 15,16). These included a relatively narrow freezing range, the minimum γ' volume fraction commensurate with strength requirements, a low γ' solvus temperature and a minimum quantity of potentially embrittling impurities. In addition, several strong superalloys, currently in use or being developed for turbine disk and blade applications, were evaluated on the remote chance that they might prove to be laser-weldable, although known to crack when conventionally welded. However, previous research at UTRC had demonstrated that $\gamma/\gamma' + \alpha$ eutectic superalloys could be rapidly solidified by the LASERGLAZE Process so as to produce unusually strong, crack-free surface layers. This suggested that alloys of this type would respond similarly when laser welded or utilized for the LAYERGLAZE Process. Previous experience at United Technologies with the nickel-rich region of the nickel-aluminum-molybdenum alloy system (Refs. 13,18) also indicated that variations of the composition of alloy MMT 143 (Ref. 17) (Ni-13 a/o Al-9 a/o Mo-2 a/o Ta) might also be laser-weldable. Such alloys could be expected to possess additional sources of creep strength at or below 760°C through the precipitation hardening of the γ by Ni_3Mo or similar intermetallic compounds, and through solid solution strengthening of the γ' by tantalum. Many alloy compositions based on this rationale, together with the more conventional alloys mentioned earlier, were laser-welded in the as-chill cast state and examined for cracks. The results achieved to date are presented in Table II.

The list of alloys tested to date and their cracking response after 1 MW/cm^2 CO_2 laser welding at 5 cm/s is documented in Table II. This data was used as the principal means of screening prospective alloys for subsequent laser deposition, since only those which remained crack-free and possessed a relatively high as-welded microhardness were scheduled for further evaluation. The surfaces of several different specimens after welding are shown in Fig. 27. Most of the cracked specimens tended to have crack patterns oriented transverse to the welding direction and these cracks frequently propagated across many overlapping weld beads (Figs. 27b and 27c). Transverse fusion zone cracks were also observed during preliminary experiments in which a single welding pass was made in crack-prone alloys, and thus are not a unique characteristic of overlapping fusion zones. In a few instances, cracking along the center line of the fusion zone was also observed (Fig. 27d). The cause of this difference in crack orientation was not apparent, although transverse section metallography suggested that all cracking was predominantly intergranular.

Observation of the as-welded surface structure at higher magnification revealed features which were common to all specimens: striations marking the successive location of the solid-liquid interface, and slip lines on the fusion zone surface caused by plastic accommodation of the solidification shrinkage (Fig. 28).

The fusion zone of all alloys (Figs. 27-32) exhibited a much finer dendritic structure than that of the unwelded chill casting below it, indicative of the higher solidification rate inherent in laser welding. When cracks were intersected by a transverse plane of observation (Fig. 30), they displayed more of a center line orientation than suggested by observation of the top surface of most welds. In general, the microstructure in the fusion zone of the welded superalloys was assumed to be a close approximation of that produced by the LAYERGLAZE Process. Support for this assumption can be derived from a comparison of as-laser welded alloy 8-12-3 (Fig. 32) and photomicrographs of disk 1-8 (subsequently discussed).

Previous investigators (Refs. 15,16) have reported that the weldability of nickel-base superalloys, particularly Rene 41, can be improved by softening them as much as possible prior to welding. To determine whether this procedure would reduce the weld cracking tendency of the experimental alloys used in this program, 20 previously evaluated chill-cast alloys based on Ni-Al-Mo were annealed in evacuated quartz for 4 hrs at 1290^{o}C, then furnace cooled. They were subjected to the standard weld cracking test described previously. The degree of weld cracking observed was not reduced in comparison with the as-chill cast specimens for any alloy. In two cases, alloys 10-12-3 and 10-10.5-3, the amount of weld cracking was markedly increased as a result of the prior high temperature anneal. This was particularly disturbing in the case of 10-12-3, which had not been previously observed to crack when welded.

B. Phase Transformation Temperatures

It was assumed that the tendency of nickel base superalloys to crack when welded might be lowered by reducing the melting range and/or lowering the γ' solvus temperature. In the former case, the persistence of interdendritic or intergranular regions of liquid which might contribute to crack initiation in welded areas which were cooling to near the solidus temperature would be reduced. In the latter case, the alloy would remain free of γ' for a relatively longer time during cooling in the solid state, and thus be more able to accommodate solidification shrinkage stresses by plastic deformation without fracturing. To determine whether these mechanisms might be operative in the case of the Ni-Al-Mo base alloys, their phase transformation temperatures were determined by differential thermal analysis (DTA), as shown by Table II. Examples of the

DTA traces for two such alloys are shown in Figs. 33 and 34. The peaks indicative of the melting and freezing of an alloy of eutectic composition shown in Fig. 30 were not observed in all cases (see Table II). It is not clear at this time whether or not failure to observe eutectic peaks on the DTA trace of a particular alloy might be due to insufficient sensitivity of the apparatus in some cases. The Ni_3Mo solvus temperatures were usually observed by DTA, in which case the shape of the trace was similar to that obtained for the γ' solvus. In some instances, such as alloy 8-12-3, the Ni_3Mo solvus could only be detected by differential thermal expansion. This suggests that both the expansion and thermal effects associated with the precipitation or dissolution of Ni_3Mo or similar phases in these alloys can be difficult to detect. However, all evidence to date indicates that phases of the Ni_xMo group will be present in the γ phase at temperatures below ~800°C in any of the Ni-Al-Mo base alloys now under consideration.

The γ' solvus and melting range data in Table II do not suggest an obvious correlation between these parameters alone and the dependence of weld cracking upon alloy composition. Even for conventional alloys for which there exists extensive welding data (Refs. 15,16), those mechanisms which are proposed to explain various types of weld cracking are in the form of reasonable explanations rather than mechanisms which have been verified by experimental observations. The possible mechanism(s) which control fusion zone weld cracking in the Ni-Al-Mo base alloys investigated here remain, at this time, matters of speculation. Development of detailed explanations for these mechanisms, which is extremely desirable, unfortunately appears to be beyond the realm of the state of the art present technology. At best, long term basic research appears to be required. It can be readily seen from the data in Table II that the sensitivity of weld cracking to small changes in composition (e.g., in alloys 11-12, 11-12-0-0-5, 12-11, 12-13 and 12-15) precludes simplisitc explanations. The same can be said for the observed variation in as-welded strength of these alloys, as estimated from the microhardness data. A significant part of the research effort in alloy design during the second year of this contract will be devoted to achieving a greater understanding of the dependence of as-welded properties upon composition in the Ni-Al-Mo family of alloys.

C. Structure and Properties of LAYERGLAZE Fabricated 8-12-3 Alloy

The microstructure and mechanical properties of the 6.45 cm (2.54 in.) diameter disk (disk 1-8, Figs. 18-21) fabricated from alloy 8-12-3 as described previously in this report were examined in some detail. For convenience, the nomenclature used to describe the planes and directions of the samples prepared from this disk are those of the cylindrical coordinate system, referred to the external disk geometry, as shown in Fig. 35. The microstructure of disk 1-8 was examined by sectioning it parallel to the r, z, and θ faces (Figs. 36-41).

This revealed that solidification occurred by dendritic growth in all areas, with little or no observable side branching (Fig. 36b). Some interdendritic phase(s) could be observed at 1000X, which indicated a greater degree of segregation and a lower cooling rate than had been expected (Ref. 18). The mean spacing of the secondary dendrite arms, both near the disk substrate and near its outer surface, was 1.9 μm (7.5×10^{-5} in.); while the mean primary dendrite spacing measured at these same locations was 3.8μm (1.5×10^{-4} in.). Comparison of these data with published observations of dendrite and dendrite arm spacings as a function of solidification rate (Ref. 18) suggest that disk 1-8 solidified at ~10^4 ^{o}C/s throughout its fabrication.

On the Z and θ faces, photomicrographs taken at positions of increasing radius did not reveal any change in grain shape or size from near the disk substrate to its outer surface. The grains were markedly elongated in a direction parallel to the disk radius, and appeared to have formed by successive epitaxial solidification as each layer was deposited. The mean grain boundary spacing measured along a line perpendicular to the disk radius was 55μm (~0.002 in.) on both the θ and Z faces. The observed grain lengths in the radial direction ranged from 127 to 1020μm (0.005 to 0.040 in.) with a mean of 660μm (0.026 in.). Striations were visible on the Z and θ faces (Figs. 37-41) which marked the position of the solid-liquid interface when each successive layer of metal was deposited. The distance between striations (~70-113μm, 0.0028-0.0045 in., Table III) is the thickness of each deposit which was not remelted during the deposition of the next layer.

Some widely-spaced porosity and inclusions were observed in the microstructure. These were spherical in all cases, and were ≤25μm (0.001 in.) in diameter, with an average spacing of 1.8 mm (0.07 in.) in the plane of observation.

Examination of the microstructure of disk 1-8 by transmission electron microscopy is still in progress. However, the observations made to date confirmed the evidence in the 1000X micrographs, in that a significant volume fraction of an as-yet unidentified interdendritic, discontinuous second phase was present in the as-solidified structure (Fig. 42). There were large numbers of uniformly distributed dislocations, predominately on {111}, within the grains and subgrains. Most of the interdendritic areas were delineated by subboundaries. The small dendrite spacing and the high dislocation density, presumably the result of accommodation of the solidification shrinkage by plastic deformation, suggest that a rapid, high-temperature anneal of the disk might provide a means of achieving both greater chemical homogenity by diffusion and grain structure refinement by recrystallization.

Both the γ' size (~20 nm) and spatial distributions were observed to be very homogeneous. A still finer phase tentatively identified as DO_{22} structure Ni_3Mo was also observed. No concentrations of γ' or Ni_3Mo were detected in the interdendritic areas.

The composition of disk 1-8 and of several welded chill-cast specimens were checked by wet chemical and Leco analysis. The results are presented in Table IV, and are quite close to the nominal composition of each specimen in all cases. The carbon content of all specimens, while generally lower than that of commercial turbine disk superalloys now in use, was still sufficient to allow the possibility of carbide precipitation in alloy 8-12-3 at temperatures of 538 to 760°C (1000-1400°F).

The parallel-face pieces which were cut from disk 1-8 and from which tensile specimens were prepared (Fig. 25) were radiographed by standard weld inspection procedures. The radiographs (Figs. 43 and 44) revealed detectable porosity in the form of two voids visible near the edge of one specimen (#8, Fig. 42), and none in any of the other eight. These observations are consistent with the absence of any porosity of similar size in the light micrographs of disk 1-8 (Figs. 35-40). In order to obtain an estimate of the density of alloy 8-12-3 as consolidated by the LAYERGLAZE Process, the density of one of the specimens shown in Fig. 42 was determined to be 9.146 g/cm^3 (0.330 lb/in^3). The strength and ductility of the tensile specimens prepared from disk 1-8 are presented in Table V. The engineering stress-strain curves for the room temperature tests were quite nominal, and are illustrated by Fig. 45. There was no detectable variation in mechanical properties with tensile specimen size. There was no statistically significant difference between the strength of the radial and axial specimens at room temperature, despite the marked elongation of the grains in the radial direction. This result can be attributed to the fine dispersion of γ' and Ni_3Mo precipitates, which control the deformation so effectively that the influence of grain shape cannot be observed.

The strength and ductility of the specimens tested at 538 and 704°C (1000 and 1300°F) were dependent upon load orientation with respect to the microstructure of the disk. The axial specimens were oriented so that the direction of loading was perpendicular to the radial direction of the disk, and thus to the predominate direction of grain elongation and dendritic growth as well. It is reasonable to assume these specimens exhibited a pronounced decrease in percent elongation and strength with increasing temperature because of interdendritic and/or intergranular precipitation of a brittle phase at test temperature. The excellent ductility and smaller decrease in strength with increasing temperature of the radial specimens is consistent with their orientation, which lies parallel to, and is much less sensitive to, the potential path of interdendritic or intergranular fracture. As mentioned previously, it is probable that a brief anneal at a temperature above the γ' solvus would have improved the chemical homogenity and refined the grains of disk 1-8. Thus there exists the potential for significantly improving the observed strength and ductility of the axial tensile specimens at 538 and 704°C (1000 and 1300°F).

TABULATION OF IMPORTANT RESULTS AND CONCLUSIONS

A. Processing

1. A LAYERGLAZE processing apparatus capable of producing fabricated parts of sizes in excess of the contract goal of 12.7 cm diameter has been fabricated, tested, and utilized to produce such parts for mechanical test evaluation.

2. A commercially available wire feeder has been adapted for the production of LAYERGLAZE parts using wire as a feedstock.

3. A simple, vibration/gravity controlled powder feeder has been designed, fabricated, and successfully used in the production of LAYERGLAZE parts using powder as a feed stock.

4. Critical parameters have been defined and "first-order" optimized for both wire fed and powder fed LAYERGLAZE processing. Important criteria are:

   a. Beam energy distribution
   b. Beam power density and power
   c. Feedstock mass flow rate
   d. Continuity (smoothness) of deposition
   e. Spatial location of feedstock impingement point relative to beam
   f. Angle of feedstock at interaction point

5. "First Order" optimized parameters used for production of LAYERGLAZE test parts were:

   a. An unstable resonator optical beam
   b. 0.78×10^5 w/cm^2 at the interaction zone (6.0 kW)
   c. 0.10-0.20 gm/sec
   d. Fine deposition increments preferred - establishing powder feed as being highly preferable to wire feed
   e. Feedstock must impact mandrel within two feedstock diameters of the edge of the beam impingement point
   f. Feedstock angle should approximate 30°.

6. The effects of power density on fusion zone shape were documented experimentally.

7. Specific geometrical operating parameters for both wire feed and powder feed, including rotation speed and crossfeed rate were "first order" optimized.

8. Additional major advantages for powder feed were identified in terms of the program as follows:

a. Powder feedstock is easier to manufacture in program alloys and thus can be more rapidly obtained, facilitating program iterations
b. Optical coupling efficiency with powder feed is substantially higher than with wire feed.

9. Powder size fractions between -170 and +500 mesh are required for the present fabrication process. Powder flow rate is not in direct proportion to nozzle cross sectional area due to flow friction and boundary layer effects.

10. A LAYERGLAZE buildup in the form of a ring with a cross section of approximately 1.9 x 2.5 cm and an inner diameter of 3.8 cm was LAYERGLAZE fabricated with powder feed from alloy 8-12-3 with good structure and excellent integrity, as demonstrated by mechanical tests. This sample showed a strong tendency for epitaxial growth, to the point of approximating a layered, radial directionally solidified structure.

11. A full size LAYERGLAZE disk preform 13.2 cm in diameter ~3 cm thick was successfully fabricated from alloy 8-12-3 and IN-718. The structural integrity of the 8-12-3 portion was good, while the IN-718 showed Type II cracking. This fabrication exercise successfully demonstrated the LAYERGLAZE/powder feed process capability to produce a disk of such size as is needed to meet program goals.

B. Alloy Design and Development

12. A complete absence of cracking after bead-on-plate laser welding with overlapping fusion zones has proved to be a sufficient criterion for the compatibility of an alloy with the LAYERGLAZE Process.

13. Several superalloys based on the Ni-Al-Mo system have been shown to be both laser weldable and stronger than conventional, weldable nickel base superalloys.

14. Superalloys based on the Ni-Al-Mo system are strengthened at temperatures of $\leq 760^{\circ}C$ ($1400^{\circ}F$) not only by a very fine dispersion of γ', but also by precipitation of DO_{22} Ni_3Mo in the γ phase.

15. Alloy 8-12-3, composed of Ni-8 a/o Al-12 a/o Mo-3 a/o Ta, has been used to fabricate a prototype, sub-size turbine disk by the LAYERGLAZE Process using powder feed. This disk possessed a dendritic microstructure of elongated grains indicative of a radially uniform solidification rate of 10^4 $^{\circ}C/s$.

16. The mean 0.2% offset yield strength and LAYERGLAZE fabricated 8-12-3 at room temperature was 1044 MPa (151,000 psi). The mean UTS was 1288 MPa (187,000 psi) and the mean percent elongation was 28.8%. At 538°C (1000°F), the mean UTS was 1087 MPa (158,000 psi) with elongation of 44% in the radial direction and 7% along the disk axis. At 704°C (1300°F), elongation was only 2.4% along the disk axis and the UTS was reduced to 722 MPa (105,000 psi). UTS in the radial direction at 704°C was 1124 MPa (163,000 psi) with 31.5% elongation (8-12-3 is a preliminary development alloy only).

17. The small dendritic spacing, high dislocation density, and small inclusion content of alloy 8-12-3 as consolidated by the LAYERGLAZE Process suggests that considerable potential exists for improved chemical homogenity and beneficial grain refinement by means of a brief, high-temperature anneal.

18. The as-laser welded microhardness of several crack-free Ni-Al-Mo base superalloys (e.g., Ni-12 a/o Al-13 a/o Mo) suggests that they will produce stronger LAYERGLAZE Process turbine disks than those made from alloy 8-12-3.

REFERENCES

1. Breinan, E. M., C. M. Banas and B. H. Kear: Laser Skin Melting ASM Conference on Laser Surface Treatment for Automotive Applications, Detroit, MI, Feb. 17, 1976.

2. Breinan, E. M. and B. H. Kear: Surface Treatment of Superalloys by Laser Skin Melting, Superalloys, Metallurgy and Manufacture, Proceedings Third International Symposium, Claitors Publishing Div., Baton Rouge, LA, p 434 (1976).

3. Breinan, E. M., B. H. Kear and C. M. Banas: Processing Materials with Lasers, Physics Today, p. 44, Nov. 1976.

4. Breinan, E. M., B. H. Kear, L. E. Greenwald and C. M. Banas: Laser Glazing--A New Process for Production and Control of Rapidly-Chilled Metallurgical Microstructures, Society of Manufacturing Engineers Paper #MR76-867, Society of Manufacturing Engineers, Dearborn, MI, Dec. 2, 1976.

5. Walsh, J. L., E. M. Breinan and P. Gumz: Suppression of γ' Precipitation in a Laser-Melted Nickel Base Alloy, Proceedings 8th International Conference on X-ray Optics and Microanalysis, and 35th Electron Microscopy Society of America, Boston, MA, Aug. 1977.

6. Kear, B. H. and E. M. Breinan: Laser Glazing, A New Process for Production and Control of Rapidly-Chilled Metallurgical Microstructures, Proceedings Sheffield International Conference on Solidification and Casting, Ranmoor House, Sheffield Univ., July 1977.

7. Breinan, E. M. and B. H. Kear: Welding With High Power Lasers: Proceedings, 25th Sagamore Army Materials Research Conference, Bolton Landing, NY, July 17-21, 1978.

8. Kear, B. H. and E. M. Breinan: Laser Processing of Materials, ibid.

9. Breinan, E. M.: Laser Materials Processing, McGraw-Hill Yearbook of Science and Technology, McGraw-Hill Book Co., New York, NY, 1978.

10. Breinan, E. M. and B. H. Kear: Rapid Solidification Laser Processing of Materials for Control of Microstructure and Properties: Proceedings Conference on Rapid Solidification Processing at Reston, VA, Claitors Publishing Div., Baton Rouge, LA, pp 87-103 (1978).

11. Kear, B. H., E. M. Breinan and L. E. Greenwald: Laser Glazing--A New Process for Production and Control of Rapidly Chilled Metallurgical Microstructures, The Metals Society, London, England, Publication #192 Solidification and Casting.

12. Greenwald, L. E., E. M. Breinan and B. H. Kear: Heat Transfer Properties and Microstructure of Laser Melted Alloys, Proceedings of the 1978 Annual Meeting of the Materials Research Society Symposium H - Laser Solid Interactions, Boston, MA, Nov. 15, 1978.

13. Breinan, E. M., E. R. Thompson, C. M. Banas and B. H. Kear: Assessment of Advanced Laser Materials Processing Technology, Report No. R77-912887-3, Final Report, Contract N00014-77-C-0418, UTRC, East Hartford, CT 06108, Nov. 30, 1977.

14. Snow, D. B. and E. M. Breinan: Proceedings of "Applications of Lasers in Materials Processing", April 18-20, 1979, Washington, DC.

15. Prager, M. and C. S. Shira: Welding Research Council Bulletin No. 128, Feb. 1968.

16. Yeniscavich, W.: The Superalloys, C. T. Sims and W. C. Hagel, eds., John Wiley & Sons, New York, 1972, p 509.

17. Cox, A. R., E. H. Aigeltinger, T. Tillman and W. K. Forrester: Quarterly Report FR-9744, UTC, Pratt & Whitney Aircraft Group, Government Products Division, Feb. 1978.

18. Mehrabian, R.: Rapid Solidification Processing, Principles and Technologies, R. Mehrabian, B. H. Kear and M. Cohen, eds., Claitor's Publishing Div., Baton Rouge, 1978, p 9.

Table I

LAYERGLAZE Operating Parameters

Parameter	1 NOL	2 Cross-Flow Initial	3 Cross-Flow Final
Beam	Gaussian	Unstable Resonator	Unstable Resonator
Power - kW	8	6	5
Focal Length - cm	45.7	45.7	45.7
Molten Pool Size - mm	2.54	1.0	3.175
Power/Area-ω/cm^2	0.16×10^5	0.76×10^5	$.063 \times 10^5$
Wire Size - mm	0.9	0.9	0.9
Wire Speed-cm/sec	2.1-7	7	.64-1.5
Arbor Surface Speed - cm/sec	5	2.1-7	2.1-17 (4.2 typ)
Advance Rate - mm/rev	0.76	0.5	1.44

Table II

Composition, Selected Properties, and Weld Cracking Response of Nickel Base Superalloys Evaluated for Layerglaze Process Turbine Disk

Alloy Identification	Alloy Composition at % (wt %)						
Ni-Al-Mo-X	**Ni**	**Al**	**Mo**	**Ta**	**Ti**	**Cr**	**Other**
8-9.5-1.5-0-5	76 (72.90)	8 (3.53)	9.5 (14.89)	1.5 (4.43)		5 (4.25)	
8-12-0-3	77 (74.95)	8 (3.58)	12 (19.09)		3 (2.38)		
8-12-1.5-1.5	77 (72.55)	8 (3.46)	12 (18.48)	1.5 (4.36)	1.5 (1.15)		
8-12-3	77 (70.3)	8 (3.36)	12 (17.9)	3 (8.44)			
9.5-9.5-0-3.5	77.5 (77.31)	9.5 (4.35)	9.5 (15.49)		3.5 (2.85)		
10-9.5-3	77.5 (72.52)	10 (4.30)	9.5 (14.53)	3 (8.65)			
10-10.5-3	76.5 (71.16)	10 (4.28)	10.5 (15.96)	3 (8.60)			
10-12-3	75 (69.16)	10 (4.24)	12 (18.08)	3 (8.52)			
11-0-5-0-20	64 (62.64)	11 (4.95)		5 (15.08)		20 (17.33)	
11-12-0-0-5	72 (71.22)	11 (5.0)	12 (19.40)			5 (4.38)	
15-5-0-0-10	70 (74.53)	15 (7.34)	5 (8.70)			10 (9.43)	
Ni-Al-Mo							
11-12	77 (75.74)	11 (4.97)	12 (19.29)				
12-11	77 (76.62)	12 (5.49)	11 (17.89)				
12-13	75 (73.70)	12 (5.42)	13 (20.88)				
12-15	73 (70.86)	12 (5.35)	15 (23.79)				
13-12	75 (74.56)	13 (5.94)	12 (19.5)				
14-9	77 (78.46)	14 (6.56)	9 (14.98)				
14-11	75 (75.45)	14 (6.47)	11 (18.08)				
14-13	73 (72.51)	14 (6.39)	13 (21.1)				
Ni-Al-Mo-Hf							**Hf**
11-12-0-0-0-2	75 (70.93)	11 (4.78)	12 (18.54)				2 (5.75)
12-13-0-0-0-2	73 (68.98)	12 (5.21)	13 (20.07)				2 (5.74)
12-13-0-0-0-4	71 (64.59)	12 (5.02)	13 (19.33)				4 (11.06)
12-15-0-0-0-2	71 (64.59)	12 (5.15)	15 (22.88)				2 (5.68)
13-9-0-0-0-2	76 (73.96)	13 (5.81)	9 (14.31)				2 (5.92)
13-12-0-0-0-2	73 (69.75)	13 (5.71)	12 (18.73)				2 (5.81)
14-13-0-0-0-2	71 (67.78)	14 (6.14)	13 (20.28)				2 (5.80)
17-11-0-0-0-2	70 (68.72)	17 (7.67)	11 (17.64)				2 (5.97)
PREVIOUSLY DEVELOPED							**C**
P&WA 643 (NX188)	72.1 (73.96)	16.97 (8)	10.74 (18)				0.19 (0.04)
MMT 143 (13-9-2)	76 (73.9)	13 (5.81)	9 (14.3)	2 (5.99)			
Mod. IN 100							
NITAC 13							
COTAC 74							
RENE 125							
COMMERCIAL							
IN 718							
ASTROLOY							
WASPALOY							
RENE 41							
RENE 62							
RENE 95							

Table II (Cont'd)

Alloy Identification	Fusion Zone Cracking				Comments	Average As-Welded Microhardness (VHN, 200)	Phase Transformation Temperatures (°C)			
Ni-Al-Mo-X	No Cracking	Slight Cracking (≤5)	Substantial Cracking	Crack Orientation			Liquidus	Solidus	γ'	Ni_3 Mo Solvus
8-9.5-1.5-0-5	*					352	1385	1357	1117	
8-12-0-3		X		Transverse		439	1371	1334	1190	
8-12-1.5-1.5		X		Transverse	All Fusion Zone Cracks Internal	418	1374	1337	1180	
8-12-3	*					420	1372	1330	1197	810
9.5-9.5-0-3.5			X	Transverse		436	1371	1341	1242	
10-9.5-3			X	Transverse		460	1382	1353	1247	
10-10.5-3			X	Transverse		523	1375	1290	1262	
10-12-3	*					518	1361	1292	1262	900
11-0-5-0-20			X	Transverse		585	1314	1272	1230	
11-12-0-0-5	*					462	1366	1292	1128	825
15-5-0-0-10			X	Transverse		394	1359	1327	1174	
Ni-Al-Mo										
11-12		X		Transverse		422	1388	1365	1140	912
12-11			X	Transverse		433	1386	1363	1173	
12-13	*					492	1377	1297	1195	913
12-15		X		Transverse		591	1365	1289	1200	907
13-12			X	Transverse		506	1377	1304	1210	911
14-9			X	Transverse		416	1391	1363	1218	
14-11			X	Transverse		474	1374	1305	1232	
14-13			X	Transverse	Cracks in Heat Affected Zone	538	1361	1304	1234	908
Ni-Al-Mo-Hf										
11-12-0-0-0-2		X		Transverse						
12-13-0-0-0-2			X	Transverse						
12-13-0-0-0-4			X	Transverse	Fusion Zone Spalled					
12-15-0-0-0-2			X	Transverse	Fusion Zone Spalled					
13-9-0-0-0-2			X	Transverse						
13-12-0-0-0-2			X	Transverse	Fusion Zone Spalled					
14-13-0-0-0-2			X	Transverse	Fusion Zone Spalled					
17-11-0-0-0-2			X	Transverse	Fusion Zone Spalled					
PREVIOUSLY DEVELOPED										
P&WA 643 (NX188)			X	Transverse	Fusion Zone Spalled					
MMT 143 (13-9-2)			X	Transverse			1374	1333	1300	
Mod. IN 100			X	Transverse						
NITAC 13			X	Transverse			1335	1265		
COTAC 74			X	Transverse						
RENE 125			X	Transverse		470				
COMMERCIAL										
IN 718		X		Transverse	Most Fusion Zone Cracks Internal	270	1335	1260		
ASTROLOY		X		Centerline						
WASPALOY		X		Centerline	Most Fusion Zone Cracks Internal	293	1355	1330		
RENE 41			X	Transverse	All Fusion Zone Cracks Internal	329	1315	1370		
RENE 62		X		Transverse	Most Fusion Zone Cracks Internal	288				
RENE 95			X	Centerline	Most Fusion Zone Cracks Internal	429				

Table III

Thickness of Individual Deposited Layers, Disk 1-8, Alloy 8-12-3

		μm	in. x 10^{-3}
Z Face:	Near Substrate	92	3.6
	Mid-Radius	133	5.2
	Near Outer Surface	74	2.9
θ Face:	Near Substrate	113	4.5
	Near Outer Surface	71	2.8

Table IV

Chemical Analysis, Selected Experimental Nickel Base Superalloys

Alloy Identification		Concentration							
		Al		Mo		Ta		C	
		at %	(wt %)	at %	(wt %)	at %	(wt %)	at %	(wt %)
8-12-3	Disk 1-8	9.85	(4.17)	12.2	(18.4)	2.85	(8.03)	0.03	(0.006)
8-12-3	Chill cast; laser welded	7.96	(3.34)	12.3	(18.3)	2.92	(8.21)	0.06	(0.012)
10-12-3	Chill cast; laser welded	9.85	(4.17)	12.2	(18.4)	3.0	(8.54)	0.10	(0.018)

Table V

Tensile Test Data, Disk 1-8, Alloy 8-12-3

Test Temperature	Specimen Identification	Orientation* Gage Diameter mm	0.2% Yield Strength MPa	(ksi)	Ultimate Tensile Strength MPa	(ksi)	% Elongation
Ambient	6A	Radial; 3.18	1055	(153)	1227	(178)	37.0
	6B	Radial; 3.18	1055	(153)	1296	(188)	31.0
	9A	Radial; 2.03	1020	(148)	1241	(180)	53.0
	9B	Radial; 2.03	979	(142)	1227	(178)	44.0
	#1 inner	Axial; 3.18	993	(144)	1255	(182)	23.9
	#1 outer	Axial; 3.18	1110	(161)	1351	(196)	12.8
	#4 inner	Axial; 2.03	1062	(154)	1324	(192)	21.7
	#4 middle	Axial; 2.03	1069	(155)	1331	(193)	13.7
	#4 outer	Axial; 2.03	1055	(153)	1338	(194)	22.0
		Mean:	1044	(151)	1288	(187)	28.8
		Unbiased Standard Deviation:	40	(6)	51	(7)	13.7
538°C(1000°F)	6C	Radial; 3.18	993	(144)	1131	(164)	40.0
	9C	Radial; 2.03	931	(135)	1069	(155)	47.0
	#2 inner	Axial; 3.18	945	(137)	1089	(158)	9.3
	#3 inner	Axial; 2.03	938	(136)	1062	(154)	5.7
	#7 middle	Axial; 2.03	931	(135)	1084	(152)	6.0
		Mean:	948	(137)	1087	(158)	44.0 (Radial): 7.0 (Axial)
		Unbiased Standard Deviation:	26	(4)	27	(4)	
704°C(1300°F)	6D	Radial; 3.18	979	(142)	1124	(163)	31.5
	#2 outer	Axial; 3.18	800	(116)	800	(116)	2.3
	#7 inner	Axial; 2.03	724	(105)	724	(105)	5.0
	#7 outer	Axial; 2.03	642	(93)	642	(93)	0
		Single Test Value, Radial:	979	(142)	1124	(163)	31.5
		Mean, Axial:	722	(105)	722	(105)	2.4

FIG. 1

LAYERGLAZE PROCESSING APPARATUS

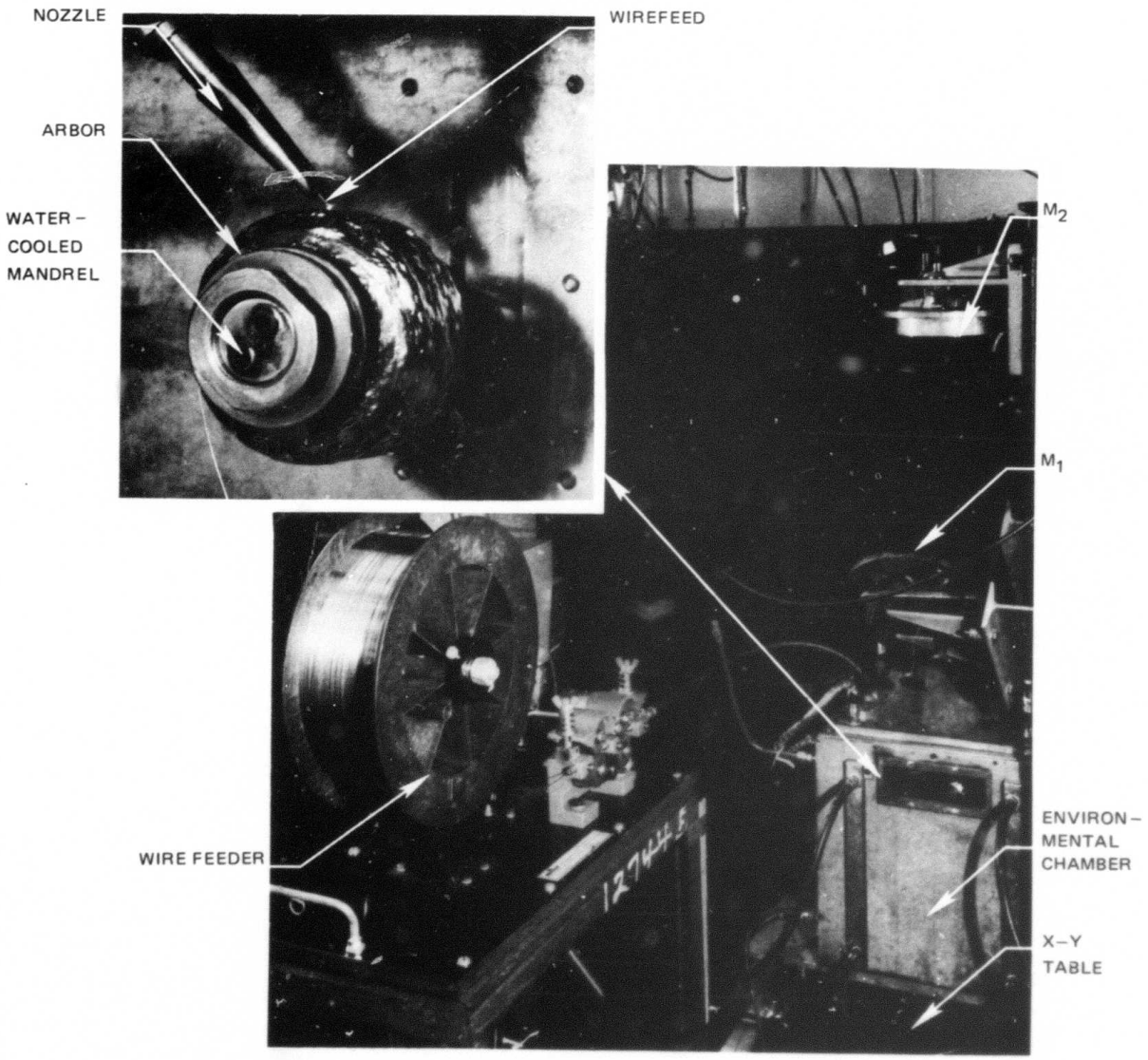

FIG. 2

AUTOMATED LAYERGLAZE PROCESSING APPARATUS

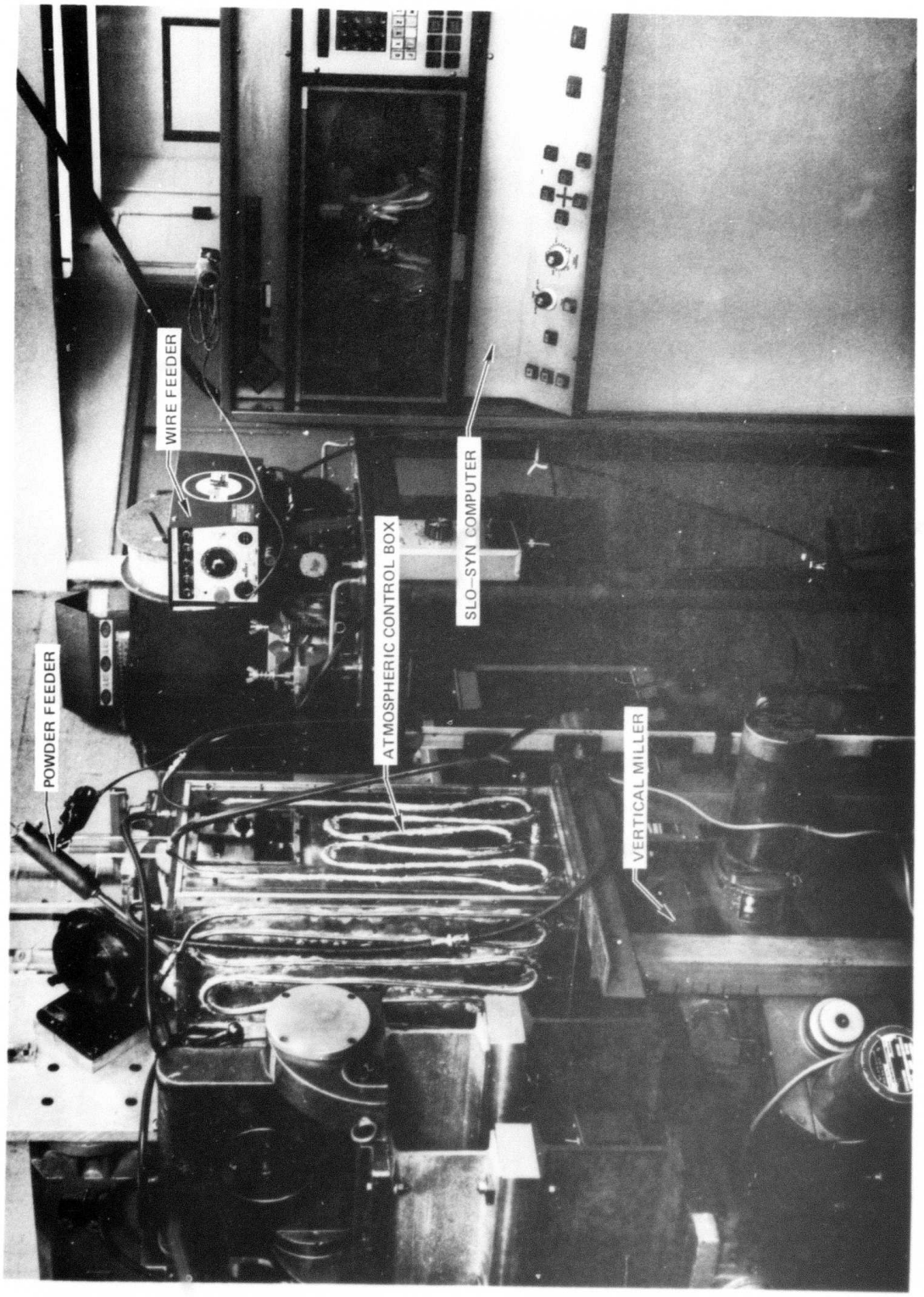

FIG. 3

LAYERGLAZE POWDER FEED FLOW TEST

- 8–12–3 SUPERALLOY
- VIBRATOR FORCED

R79-914346-4

DROP TRANSFER EFFECTS IN WIRE – FEED LAYERGLAZE PROCESS

- SINGLE LAYER
- LARGE DROPLETS

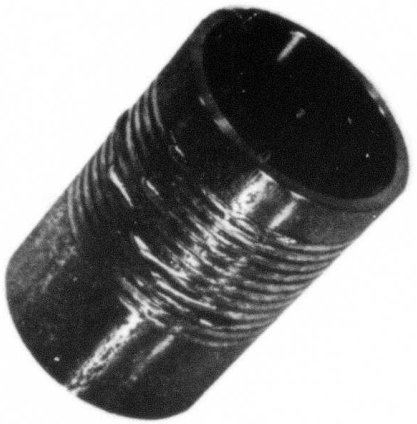

a)

- SINGLE LAYER
- NEAR OPTIMUM DROPLETS

b)

- MULTIPLE LAYER
- LARGE DROPLETS

c)

79-08-2-5

FIG. 4

FIG. 5

DETAILS OF INTERACTION REGION BETWEEN OPTICAL BEAM, ARBOR AND FEEDSTOCK MATERIAL

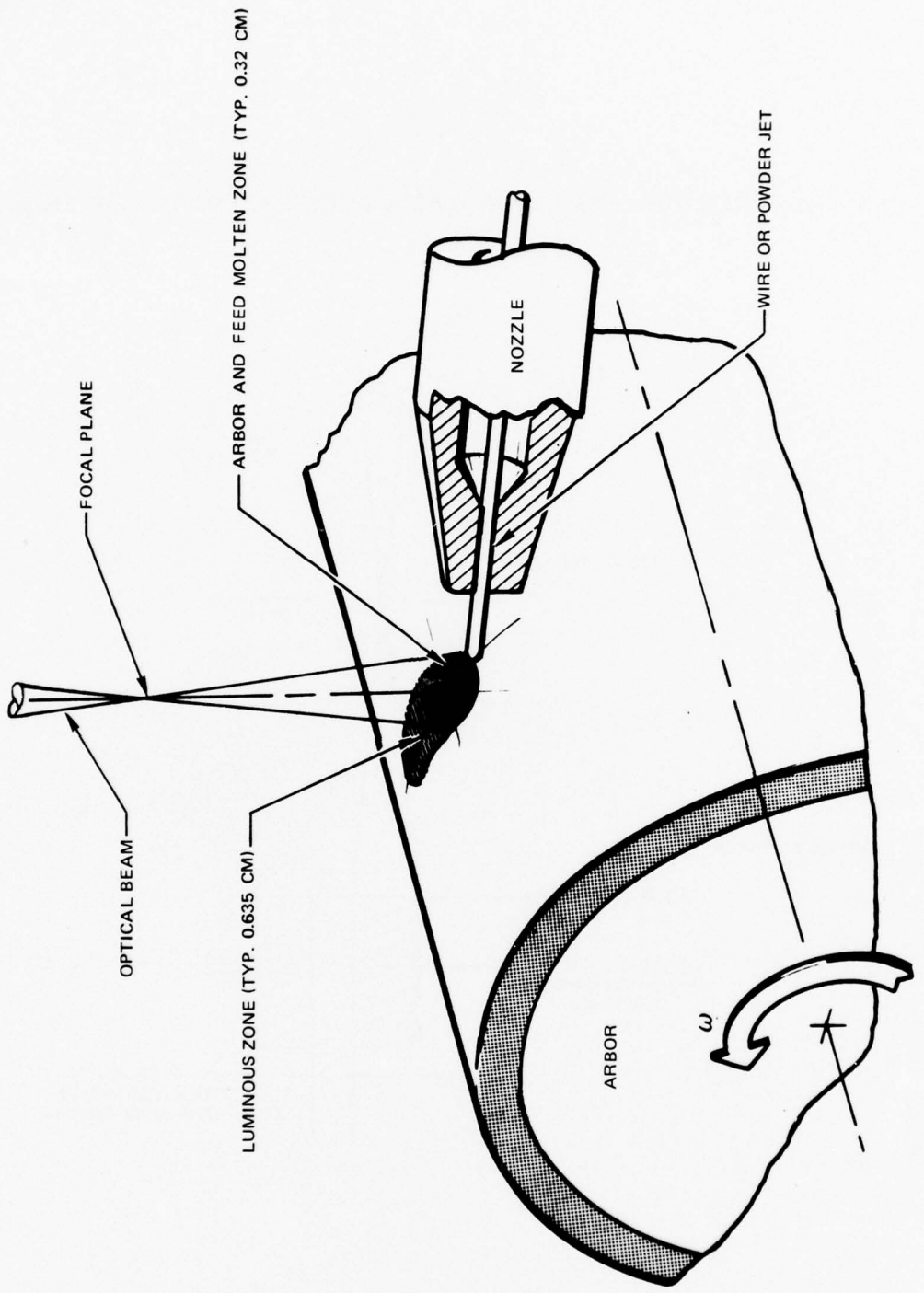

79-08-2-7

FIG. 6

STABILITY CRITERION FOR LAYERGLAZE PROCESS FEEDSTOCK INTERACTION ZONE

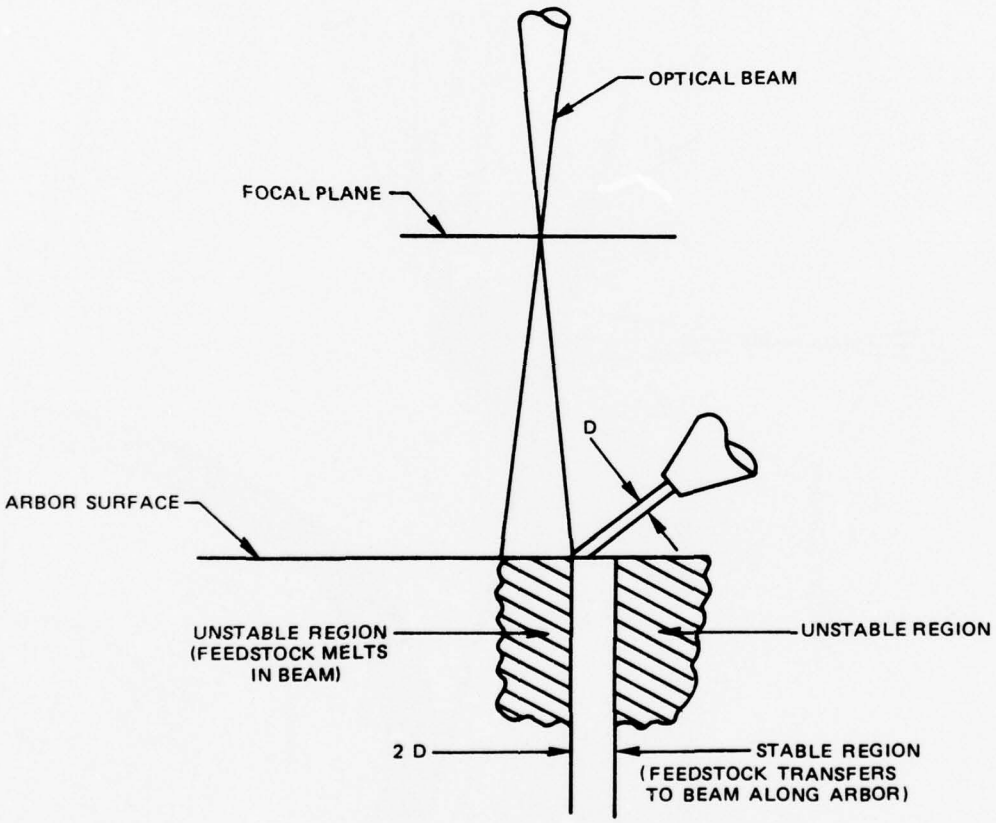

79–08–2–13

MOLTEN PROFILE AS FUNCTION POSITION

- RELATIVE SPEED – 1.3 CM/SEC
- FOCAL LENGTH – 61 CM
- OPTICAL POWER – 6 kW

58.4 CM

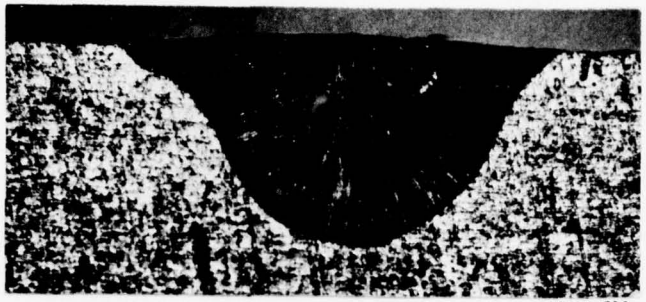

63.5 CM

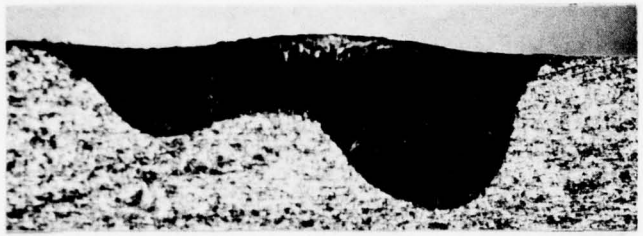

59.7 CM

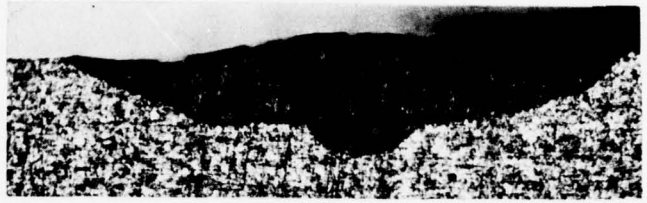

62.2 CM

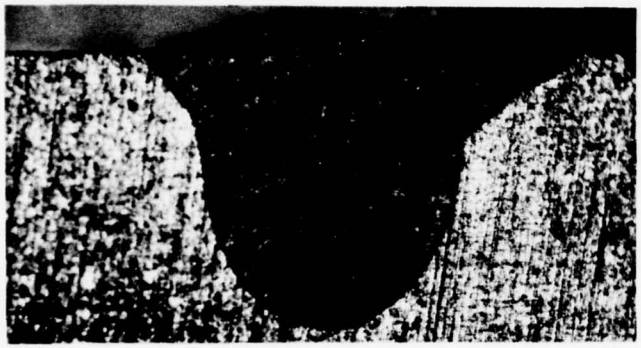

61 CM

64.8 CM

1 MM

79-08-12-18

R79-91436-4

FIG. 7

FIG. 8

SPOT SIZE AS FUNCTION OF DISTANCE FROM FOCUS MIRROR

- FOCAL LENGTH – 61 CM
- OPTICAL POWER – 6 kW
- RELATIVE SPEED – 1.3 CM/SEC

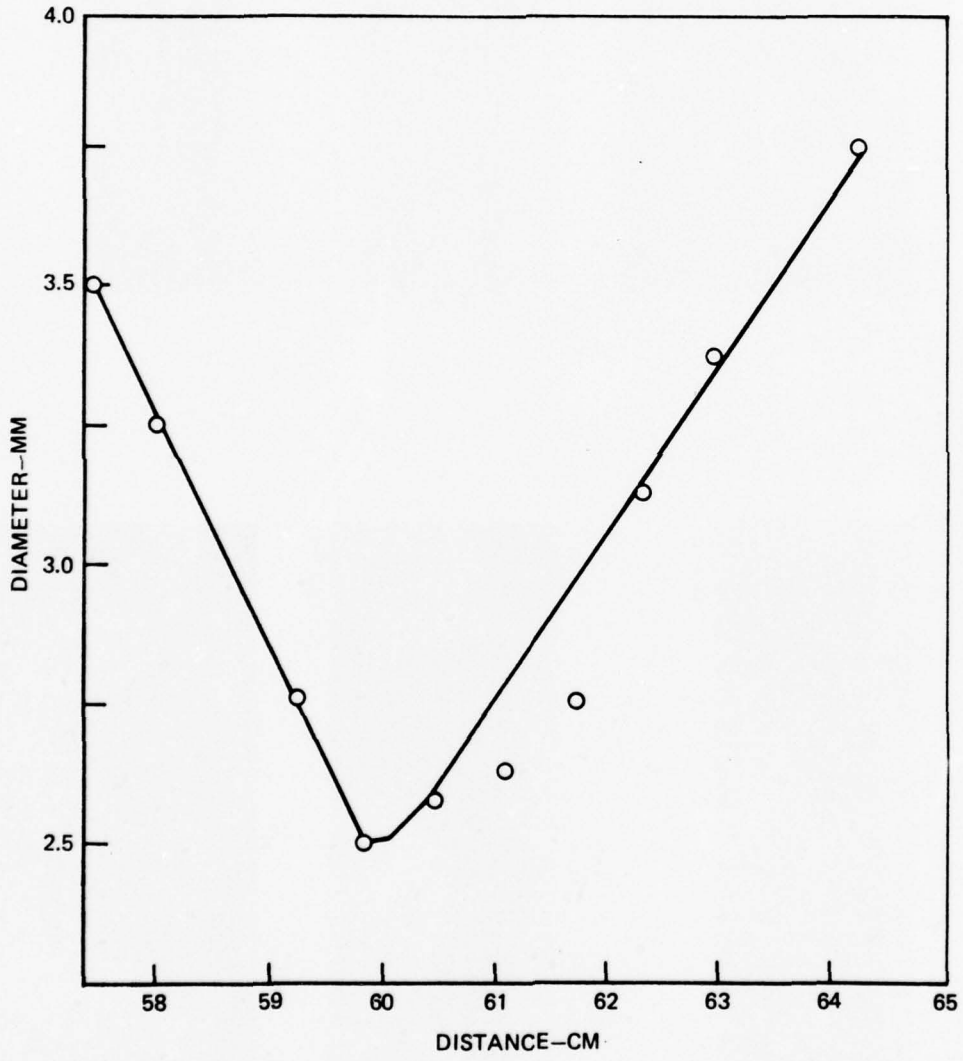

79–08–2–11

EFFECT OF CROSS FEED SPEED ON WIRE DEPOSIT

- SINGLE LAYER
- POWER–5.5 kW
- WIRE–1.5 CM/SEC
- SURFACE SPEED–4.45 CM/SEC
- SPACING–64.5 CM

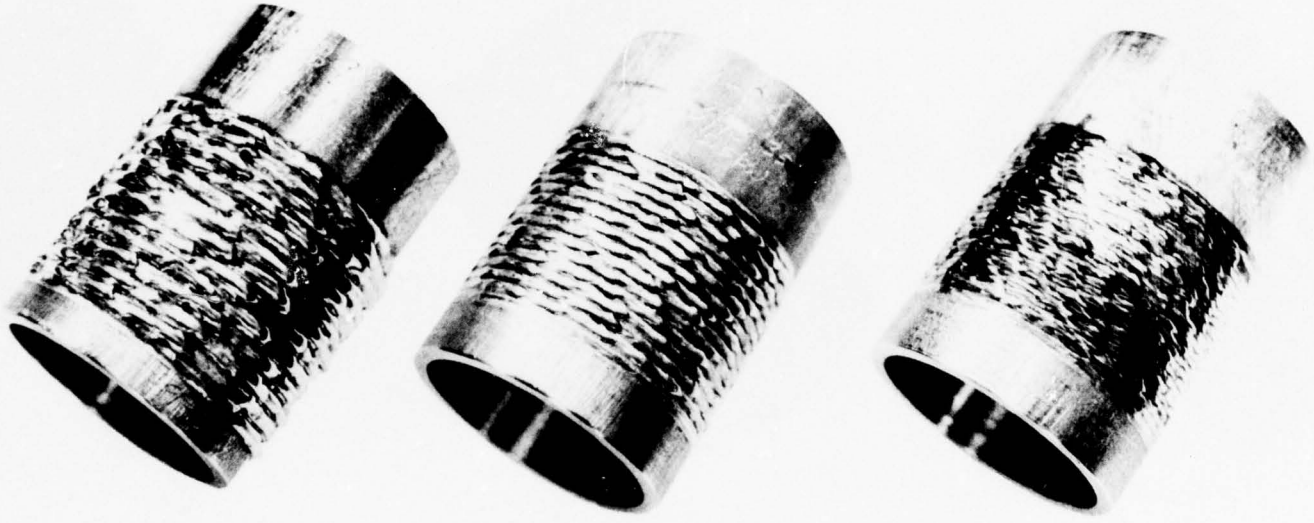

5 CM/MIN

3.8 CM/MIN

3 CM/MIN

R79-914346-4

LAYERGLAZE TEST ARBORS WITH FIVE LAYER DEPOSITS

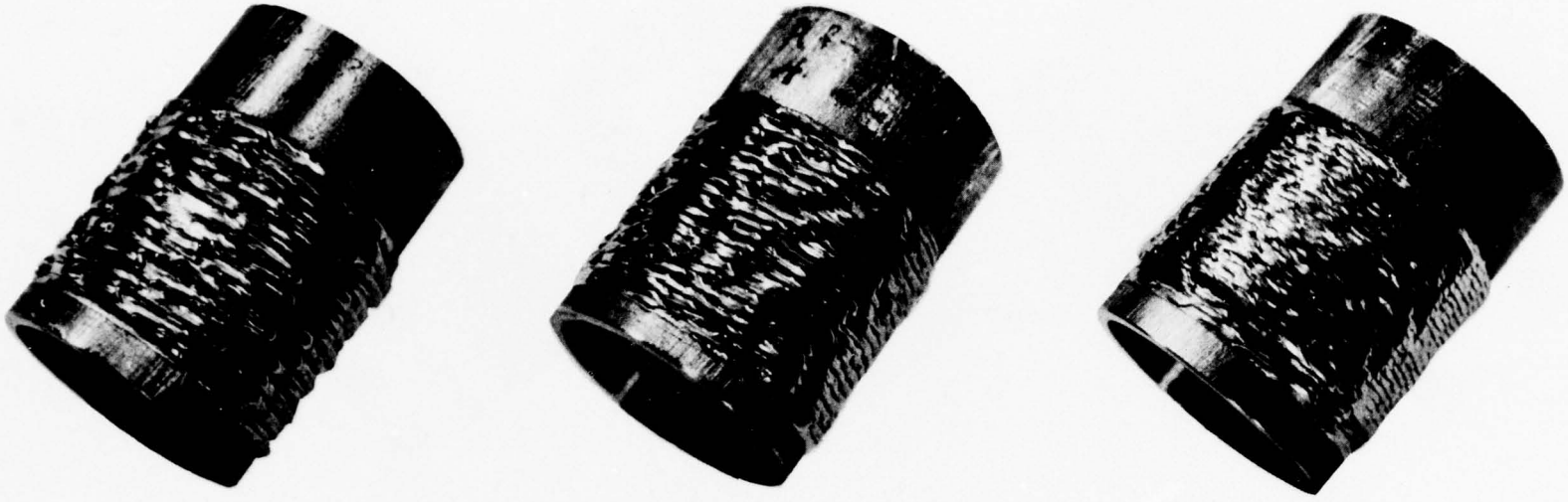

5 CM/MIN.

3.8 CM/MIN.

3 CM/MIN.

- SURFACE SPEED – 4.45 CM/SEC
- ARBOR ADVANCE RATE – AS SPECIFIED
- WIRE – 0.9 MM DIAMETER AT 1.5 CM/SEC
- LASER POWER AT WORKPIECE – 5.0 kW

79-08-2-1

FIG. 10

EFFECT OF NUMBER OF DEPOSITED LAYERS ON SURFACE APPEARANCE

- POWER–5.5 kW
- WIRE– 1.5 CM/SEC
- SURFACE SPEED– 4.45 CM/SEC
- SPACING – 64.5 CM

1 LAYER

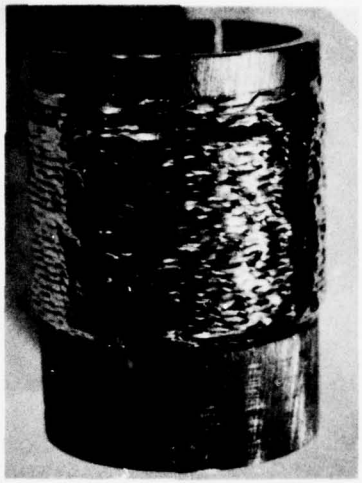

5 LAYERS

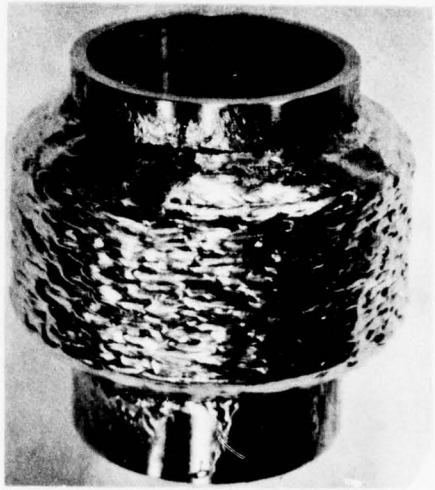

58 LAYERS

FIG. 11

FIG. 12

58 LAYER LAYERGLAZE DEPOSIT

AS DEPOSITED

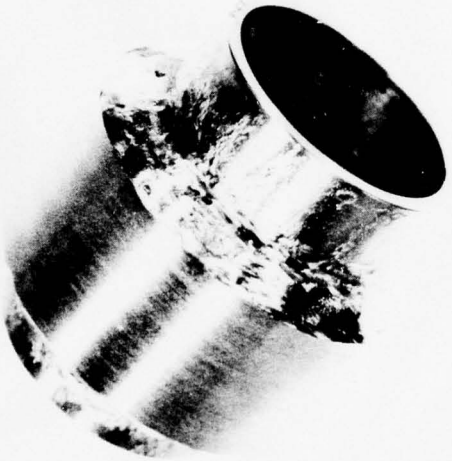

SURFACE MACHINED

79-08-2-16

FIG. 13

MACROETCHED CROSS–SECTION OF 58 LAYER DEPOSIT

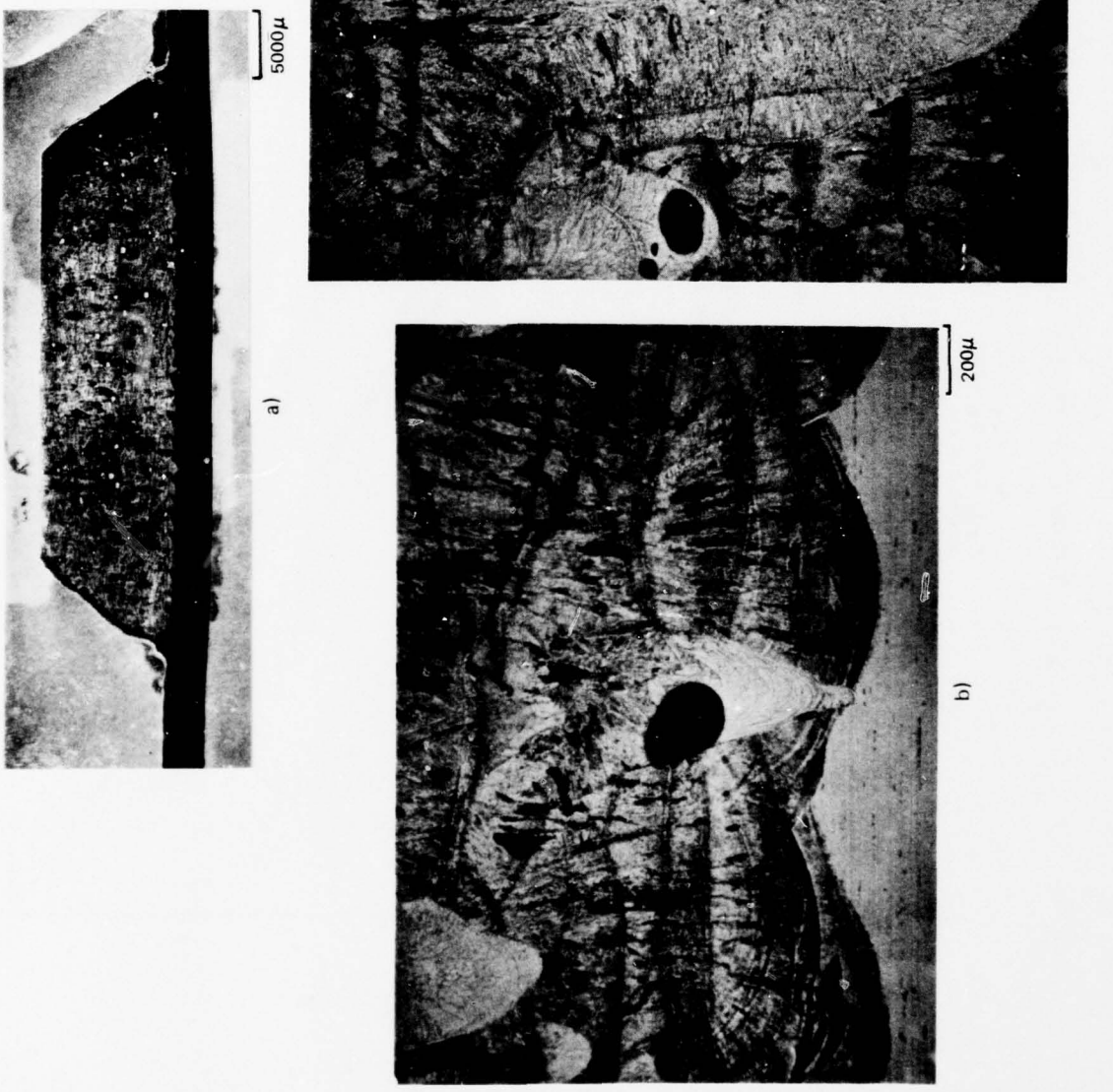

79–08–2–2

FIG. 14

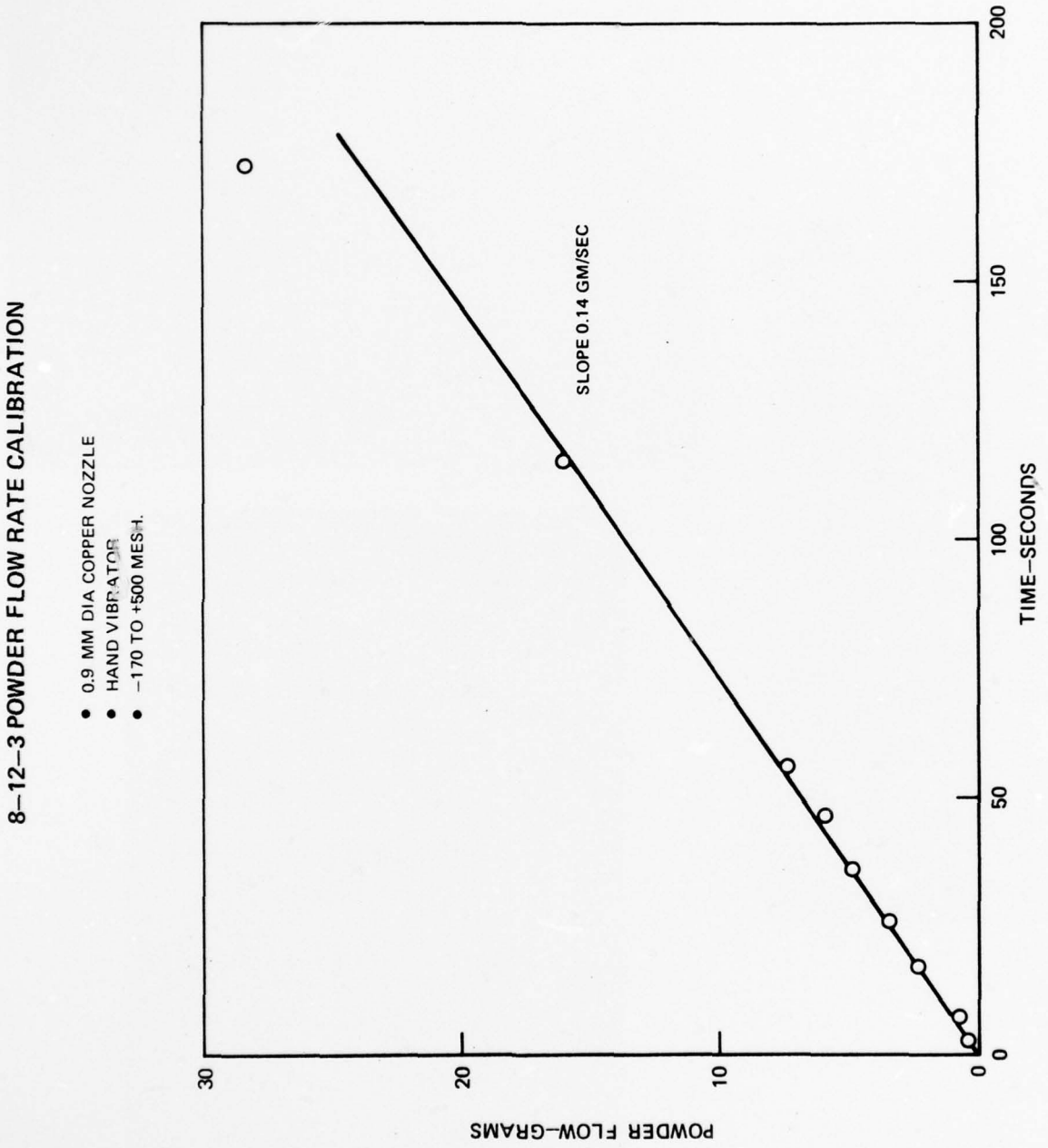

79–08–2–12

FIG. 15

LAYERGLAZE TEST SAMPLE NO. 1–6

- ALLOY: 8–12–3
- POWDER: (–170, + 500 MESH)
- POWER: 5 kW
- SURFACE SPEED: 6.7 CM/SEC

79–02–266–2

EFFECT OF LASER POWER ON POWDER DEPOSIT QUALITY

(ALL SAMPLES SAME NOZZLE DIAMETER AND TRAVERSE SPEEDS)

3 kW

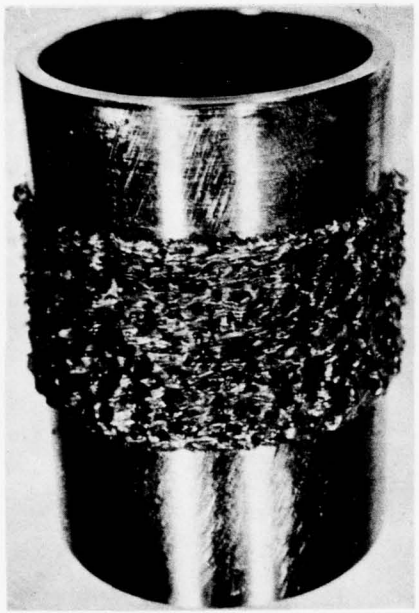

SAMPLE #2–6
- 5 LAYERS
- INCOMPLETE MELTING
- SURFACE NOT GLAZED

4 kW

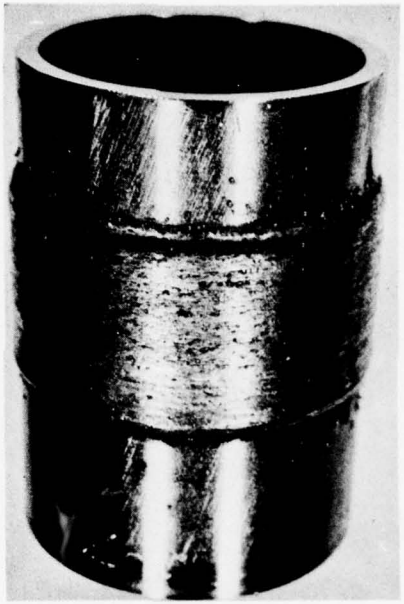

SAMPLE #2–7
- 5 LAYERS
- SLIGHT ADHERENT SPATTER
- 3/4 SURFACE GLAZED, FINAL PASS SURFACE SLIGHTLY OXIDIZED DUE TO WATER LEAK

5 kW

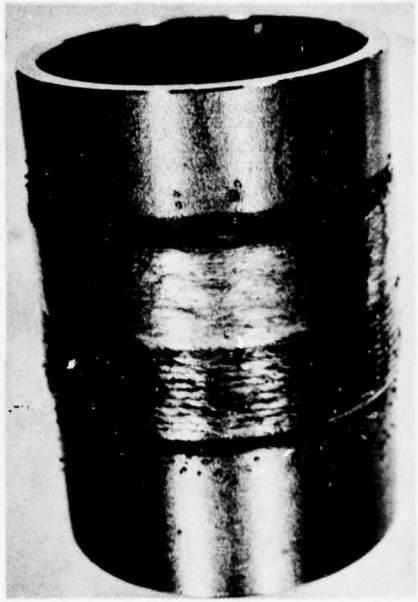

1 CM

SAMPLE #2–8
- 5 LAYERS
- LESS ADHERENT SPATTER
- 1/2 SURFACE GLAZED FINAL PASS

EFFECT OF MASS FLOW ON POWDER DEPOSIT QUALITY

(ALL SAMPLES AT 5 kW AND SAME TRAVERSE SPEEDS)

1.1 MM NOZZLE

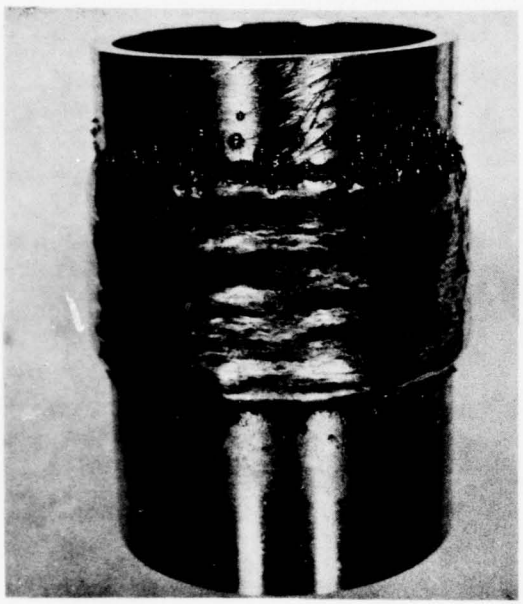

SAMPLE #2–16

- 2 LAYERS
- 0.8 MM/LAYER
- LARGE DROPLETS GLAZED ON BOTH PASSES

1.1 MM NOZZLE

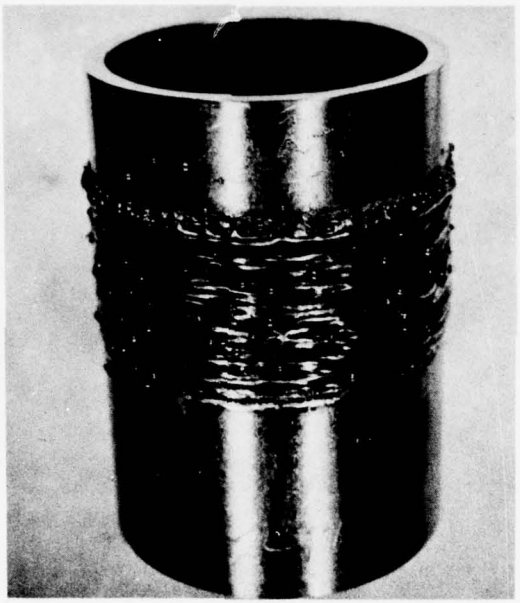

SAMPLE #2–17

- 1 LAYER
- 0.8 MM/LAYER
- LARGE DROPLETS NOT GLAZED

0.9 MM NOZZLE

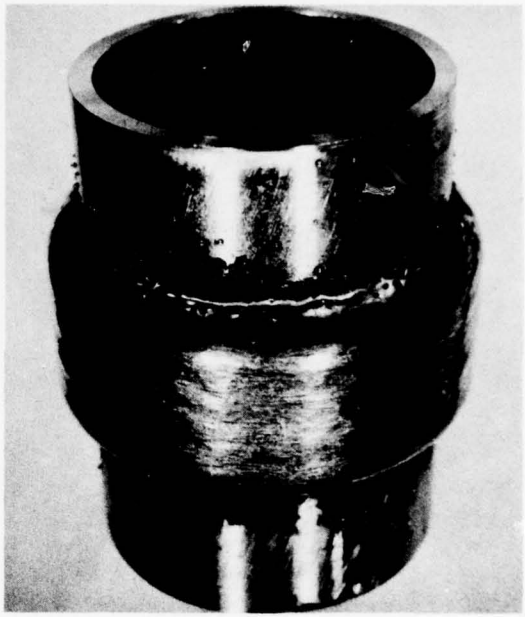

1 CM

SAMPLE #2–4

- 15 LAYERS
- 0.25 MM/LAYER
- SMALLER DROPLETS
- GLAZED ON FINAL PASS ONLY

LAYERGLAZE TEST SAMPLE NO. 1–8 AS–FABRICATED

- POWER: 5.0 kW
- SURFACE SPEED: 8.5–14.2 CM/SEC
- 8–12–3 POWDER: (–100, + 500 MESH)
- FINAL DIAMETER: 6.45 CM

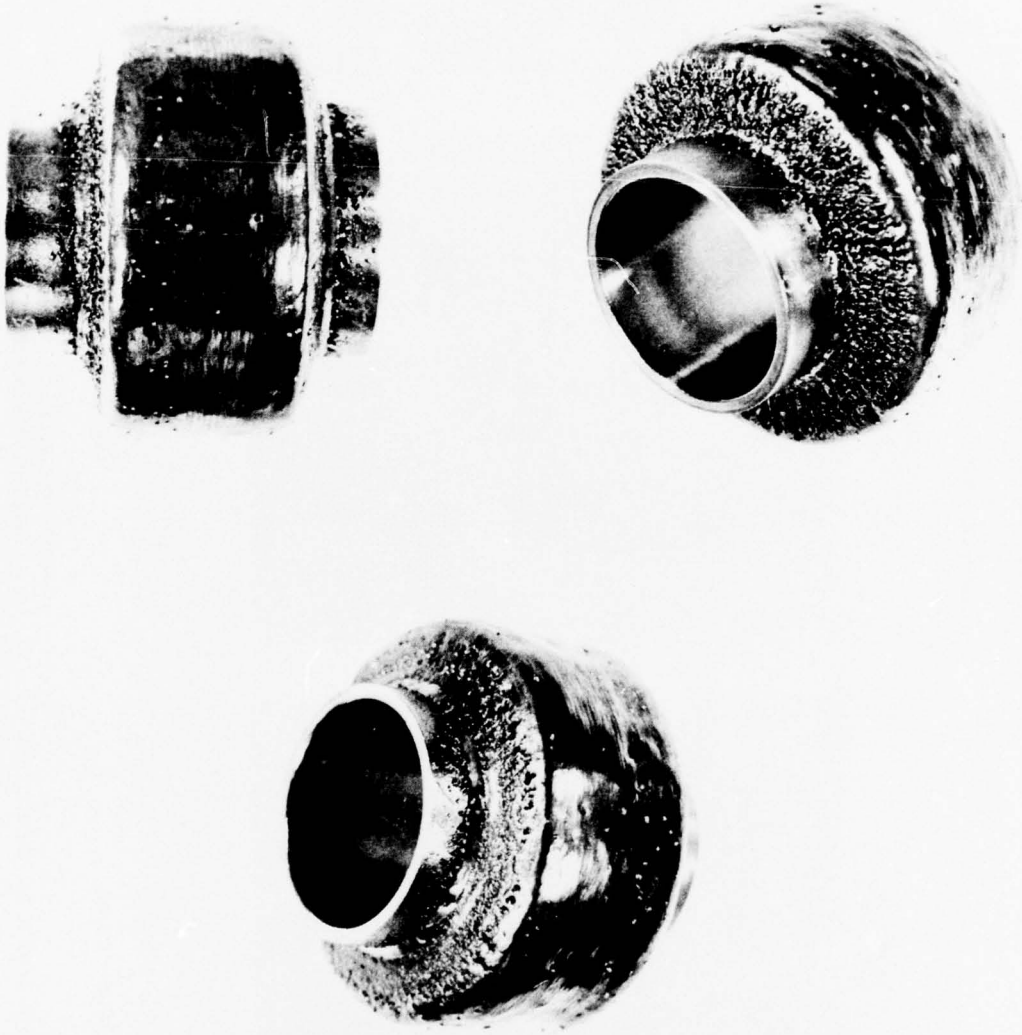

79–02–266–30

FIG. 19

LAYERGLAZE TEST SAMPLE NO. 1–8 AFTER MACHINING OF ENDS

- POWER: 5.0 kW
- SURFACE SPEED: 8.5–14.2 CM/SEC
- 8–12–3 POWDER: (–100, + 500 MESH)
- FINAL DIAMETER: 6.45 CM

79–02–266–31

CROSS SECTION OF LAYERGLAZE TEST SAMPLE NO. 1–8

(TRANSVERSE SECTION–MACROETCHED)

MACRO PHOTOS

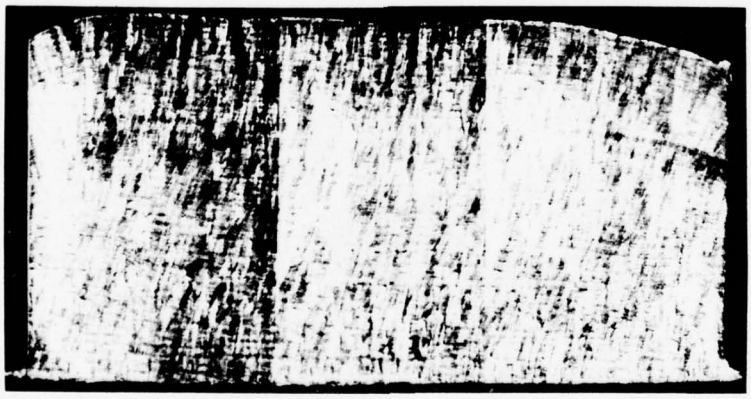

LOW MAGNIFICATION MAP OF DEPOSITED CROSS SECTION

END VIEW OF DEPOSITED MATERIAL ON LAYERGLAZE TEST SAMPLE NO. 1–8

MACRO PHOTO OF PART

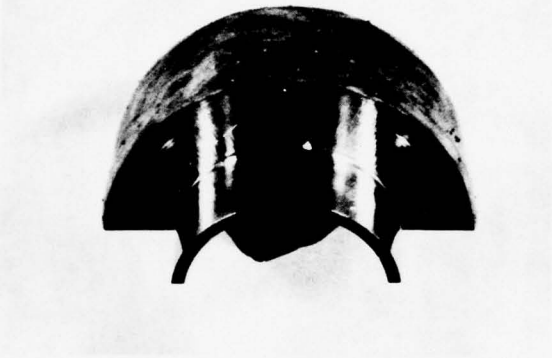

MAGNIFIED PHOTO SHOWING RADIALLY ALIGNED COLLUMNAR GRAIN STRUCTURE

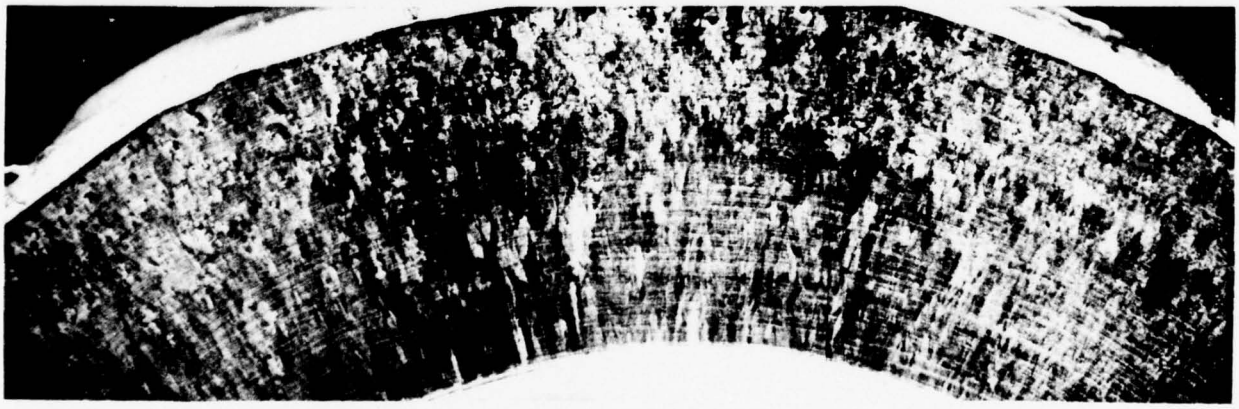

79–02–266–23

FIG. 22

LAYERGLAZE –FABRICATED TURBINE DISK PREFORM

FINAL DIAMETER : 13.2 CM

(BOTH SIDES ARE SHOWN)

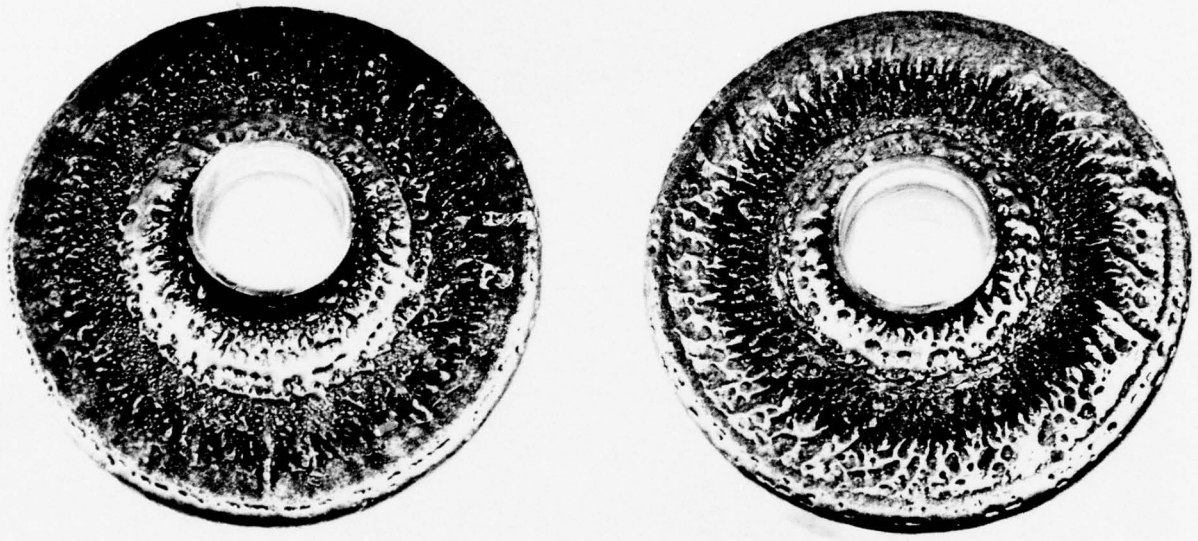

79–150–A
79–150–D

79–08–2–14

R79-914346-4

LAYERGLAZE –FABRICATED TURBINE DISK PREFORM

(MACHINED TO A ROUGH DISK CONFIGURATION AND ETCHED)

FINAL DIAMETER : 13.2 CM

AS MACHINED

PARTIALLY ETCHED

79-08-2-15

FIG. 23

FIG. 24

MACROETCH CROSS–SECTION OF LAYERGLAZE – FABRICATED TURBINE DISK PREFORM

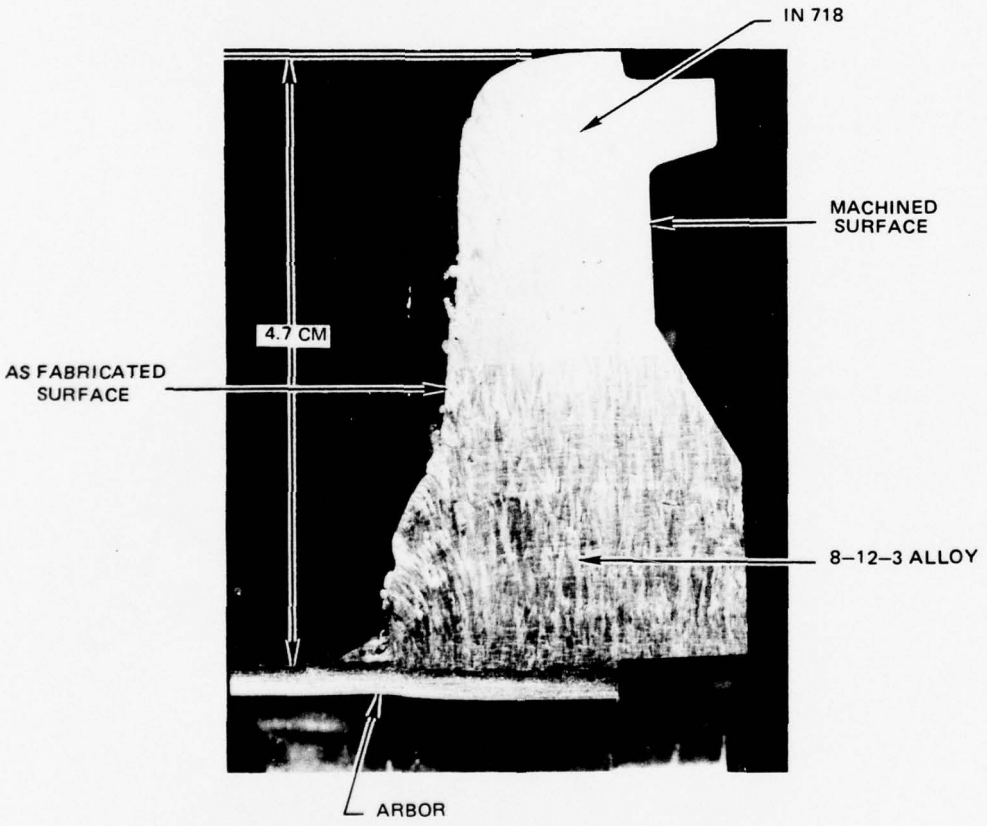

79–08–2–17

FIG. 25

PIECES SECTIONED FROM DISK 1–8 FOR RADIOGRAPHY AND TENSILE SPECIMENS

(A) VIEW EDGE–ON

(B) VIEW WITH CUT FACES FLAT

A.

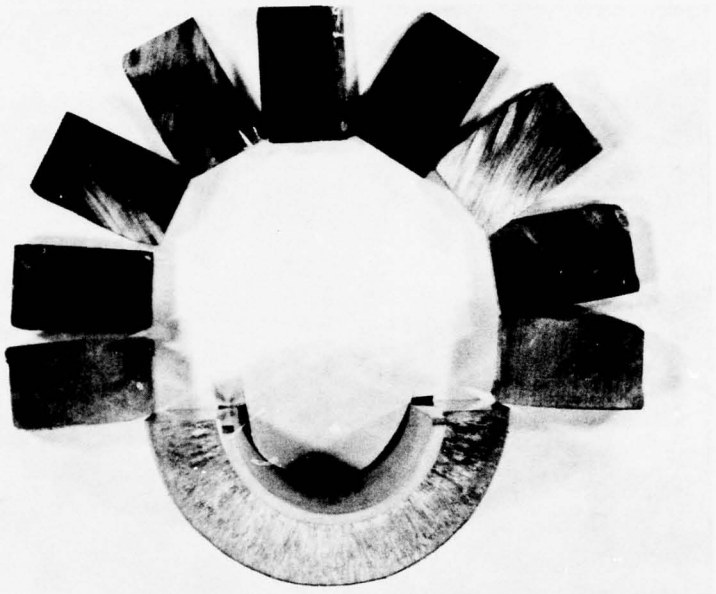

1 CM

B.

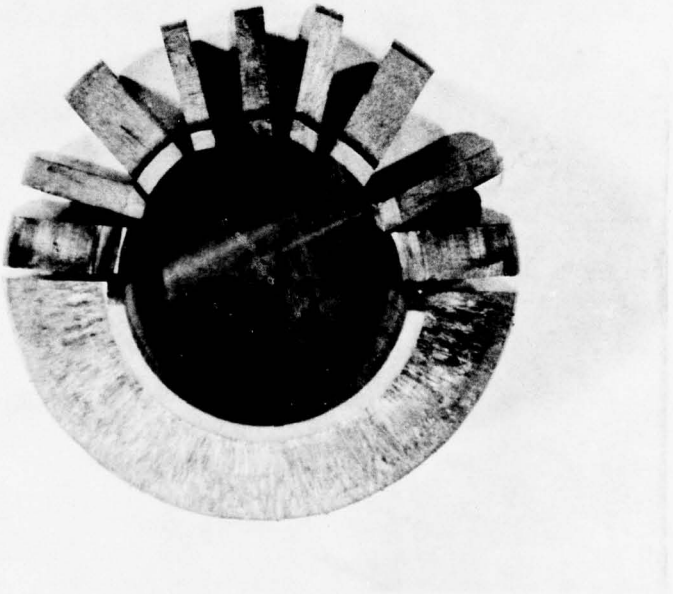

1 CM

79–08–34–14

TENSILE SPECIMENS MACHINED FROM OF DISK 1–8

SHORT SPECIMENS ARE ORIENTED PARALLEL TO THE DISK RADIUS; LONG SPECIMENS ARE PARALLEL TO THE DISK ROTATIONAL AXIS.
(A) ALL TENSILE SPECIMENS (B) ALL FOUR SIZES OF TENSILE SPECIMEN. GAGE LENGTHS ARE 7.62 AND 2.54 MM (0.3 AND 0.1 IN).
GAGE DIAMETERS ARE 3.18 AND 2.03 MM (0.125 AND 0.08 IN.)

A.

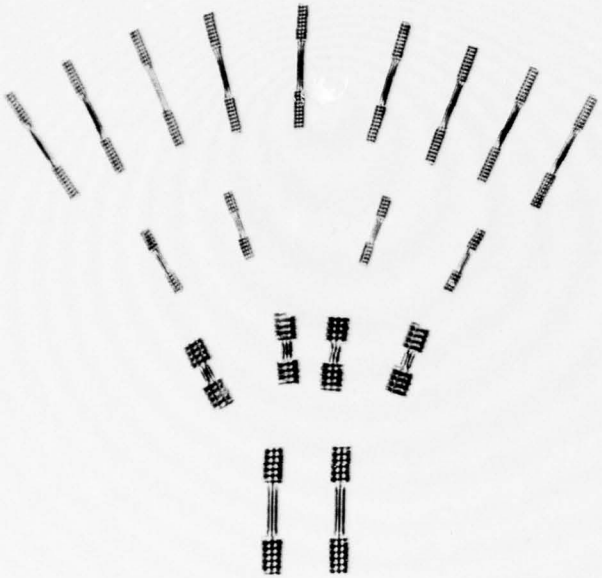

2 CM

B.

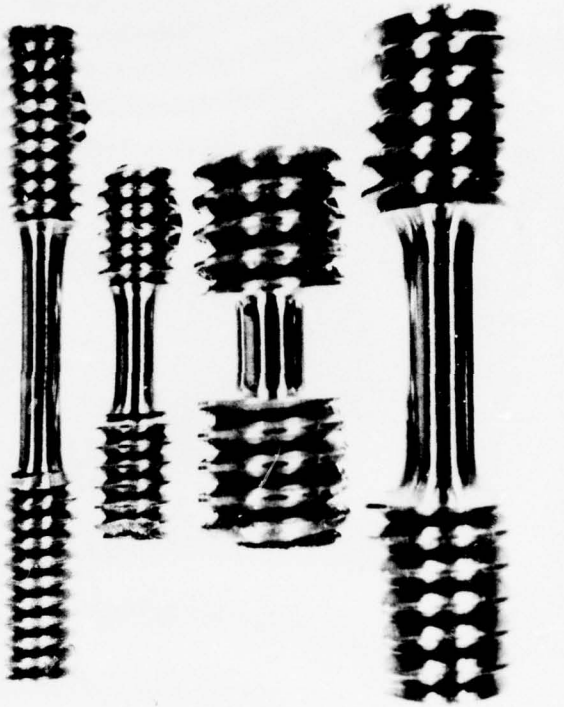

1 CM

79–08–34–15

R79–914346–4

FIG. 26

SURFACE OF VARIOUS ALLOY SPECIMENS AFTER LASER WELD CRACK TESTING

OVERLAPPING PASS BEAD–ON–PLATE LASER WELDS AT 1 mW/cm^2 BEAM INTENSITY AND 5 cm/s BEAM TRAVERSE SPEED

(A) ALLOY 10–12–3, CRACK FREE — 9 mm

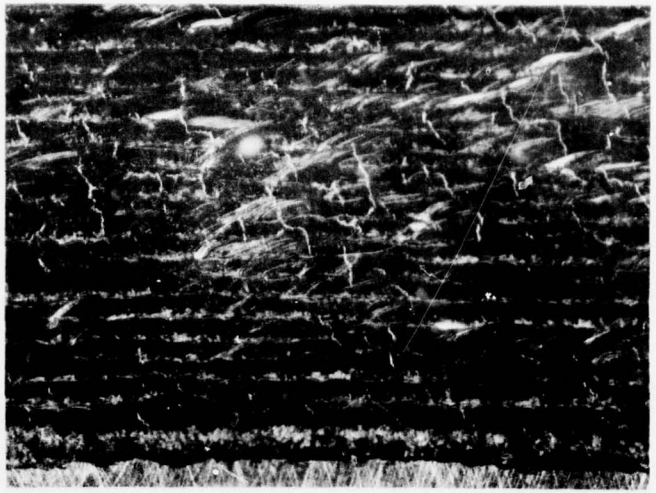

(B) ALLOY 9.5–9.5–0–3.5, TRANSVERSE SURFACE CRACKS — 7 mm

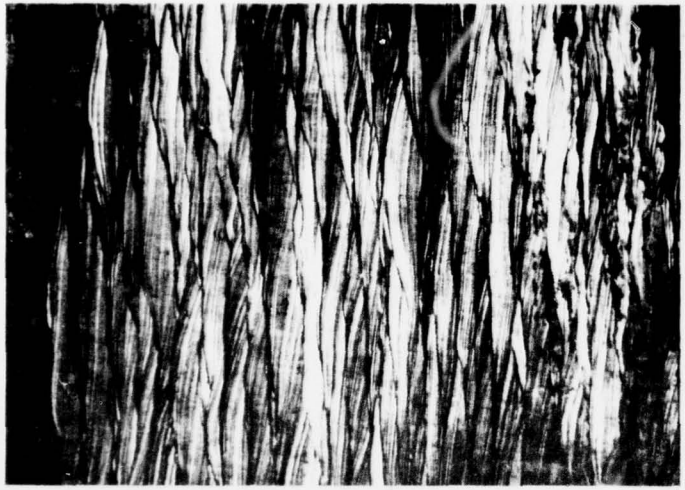

(C) RENE 62, NO SURFACE CRACKS — 7.5 mm

(D) RENE 125, LONGITUDINAL AND TRANSVERSE SURFACE CRACKS — 7.5 mm

79–08–34–23

R79–914346–4

FIG. 27

SLIP LINES ON FUSION ZONE SURFACE, ALLOY 8–12–3

LASER WELDED AT 0.5 MW/CM^2 BEAM INTENSITY AND 25 CM/S BEAM TRAVERSE SPEED

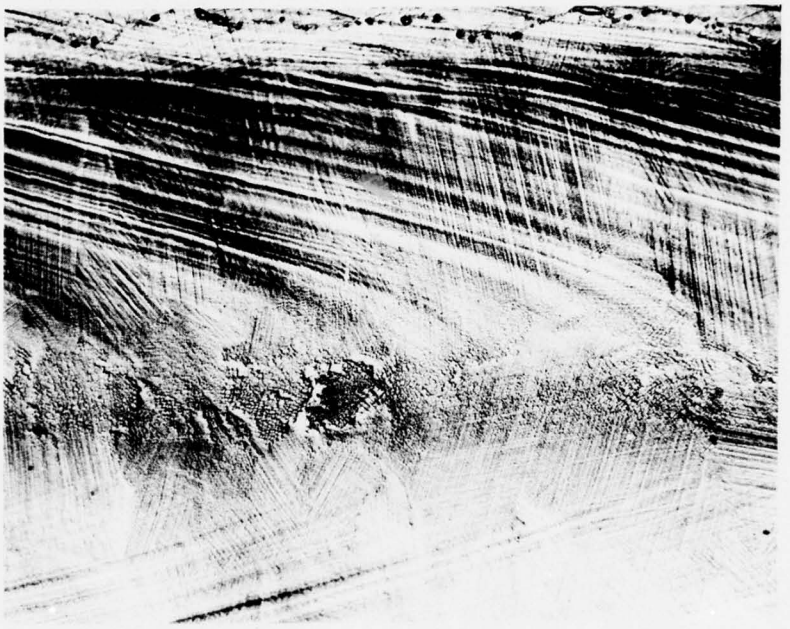

FIG. 29

TRANSVERSE SECTION OF WELD CRACK TEST SPECIMEN, ALLOY 8–12–3 (CRACK FREE)

BEAM TRAVERSE DIRECTION INTO PAGE. OVERLAPPING BEAD–ON–PLATE LASER WELDS MADE ON AS–CHILL–CAST SPECIMEN, 1 mW/cm^2 BEAM INTENSITY, 5 cm/s BEAM TRAVERSE SPEED.

79–08–34–25

CENTERLINE GRAIN BOUNDARY CRACKING

TRANSVERSE SECTION OF LASER WELD CRACK TEST SPECIMEN,
ALLOY 9.5–9.5–0–3.5

200μm

79–08–34–17

R79–914346–4

FIG. 31

TRANSVERSE SECTION OF LASER WELD CRACK SPECIMEN, ALLOY 8–12–3

AREA IN FIGURE 29 SHOWING OVERALL GRAIN STRUCTURE OF FUSION ZONE

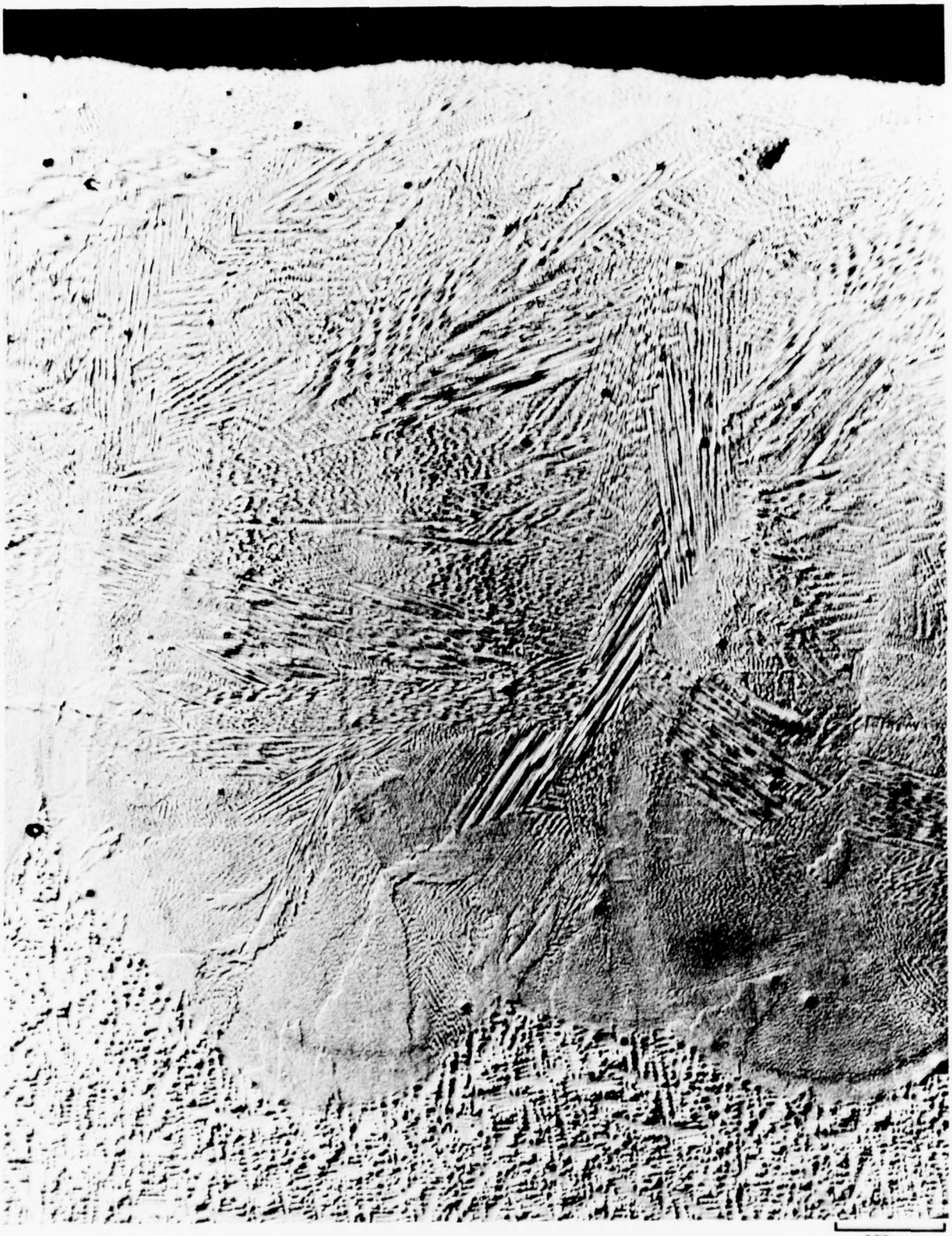

FIG. 32

TRANSVERSE SECTION OF LASER WELD CRACK SPECIMEN, ALLOY 8–12–3

AREA IN FIGURE 29 ILLUSTRATING REFINEMENT OF DENDRITIC STRUCTURE FROM CHILL CASTING (BOTTOM) TO OVERLAPPED FUSION ZONES (TOP)

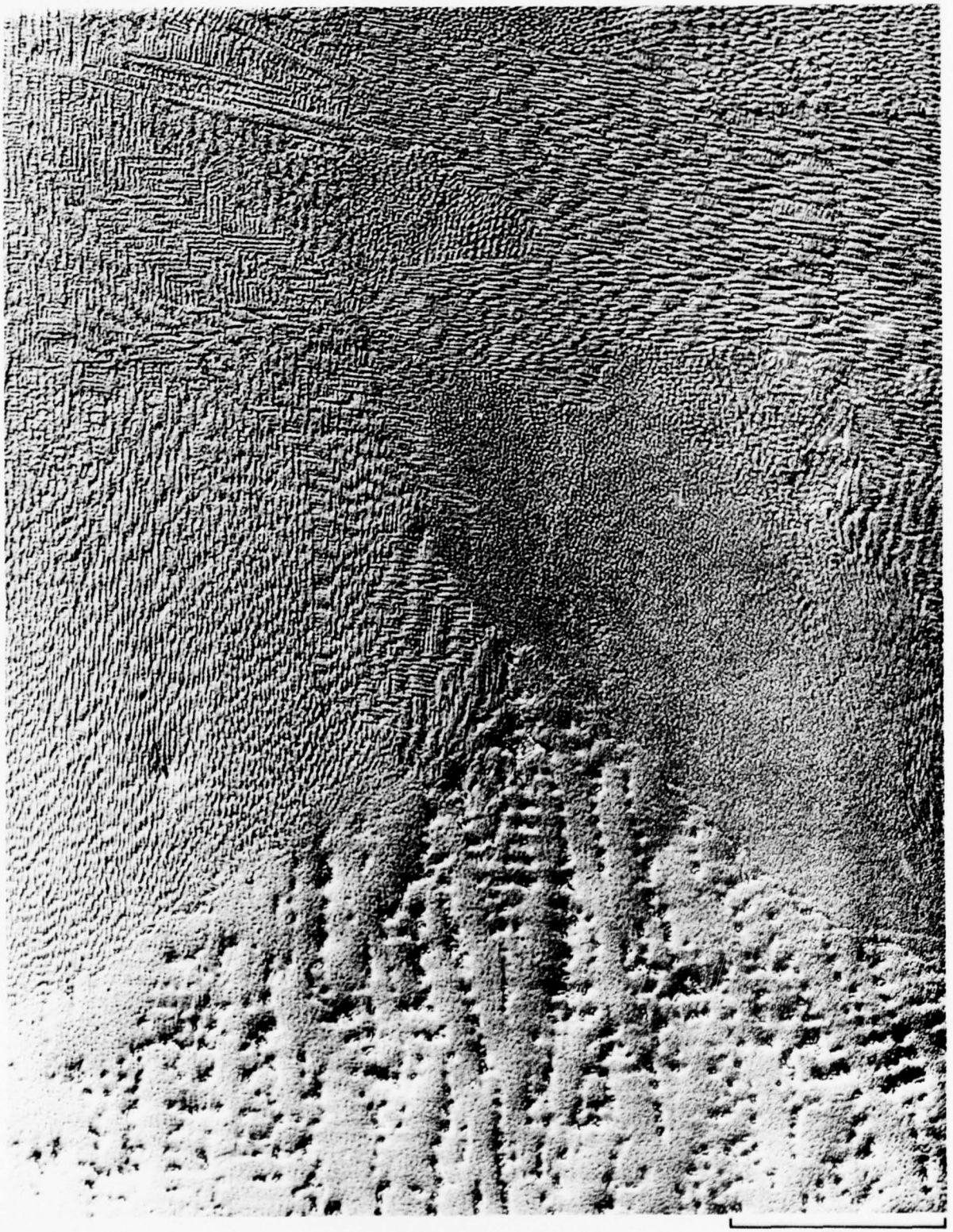

DIFFERENTIAL THERMAL ANALYSIS (DTA) TRACE FROM ALLOY 10–12–3

HEATING AND COOLING RATES, 5°C/min, PURE NICKEL STANDARD

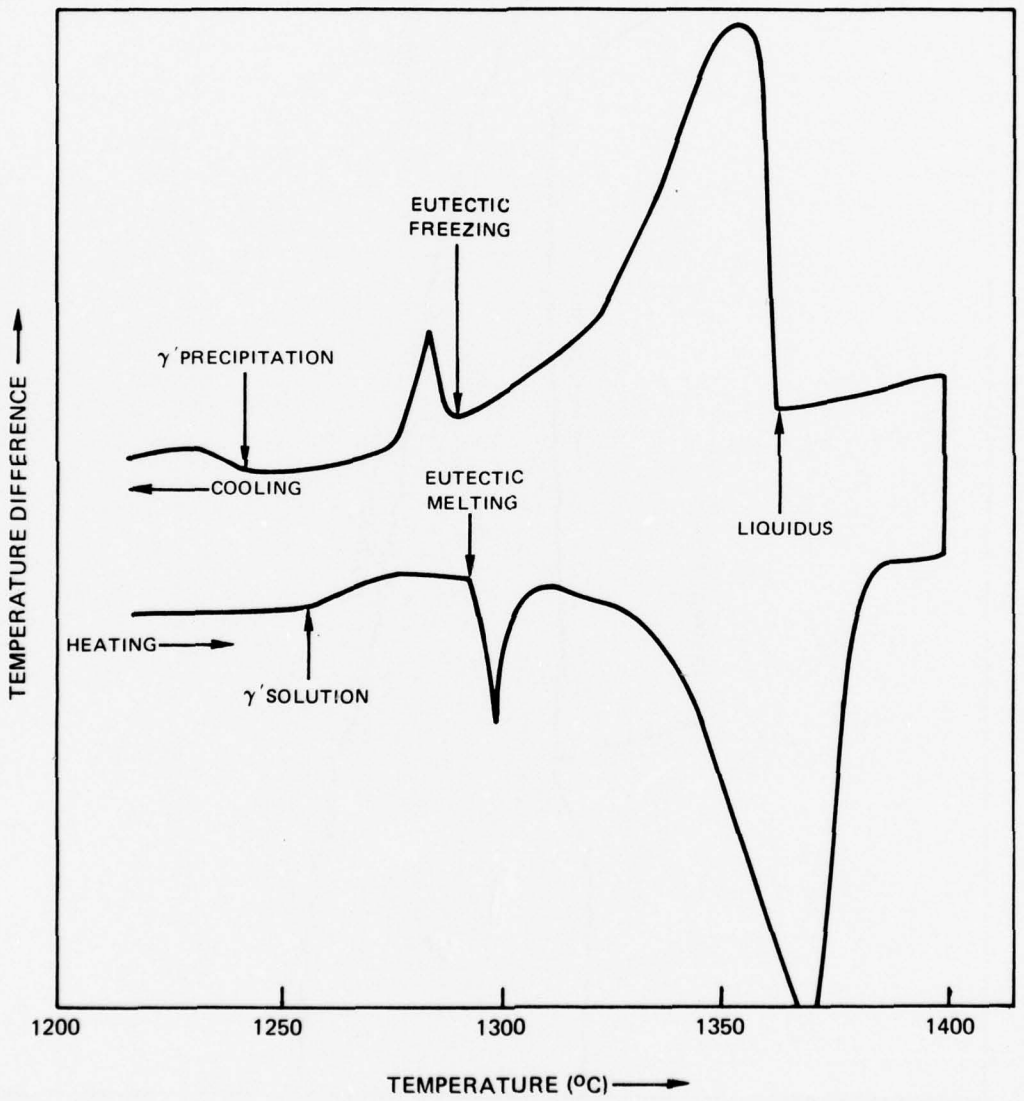

79–08–34–21

FIG. 34

DIFFERENTIAL THERMAL ANALYSIS (DTA) TRACE FROM ALLOY 12–11

HEATING AND COOLING RATES, 5°C/min PURE NICKEL STANDARD

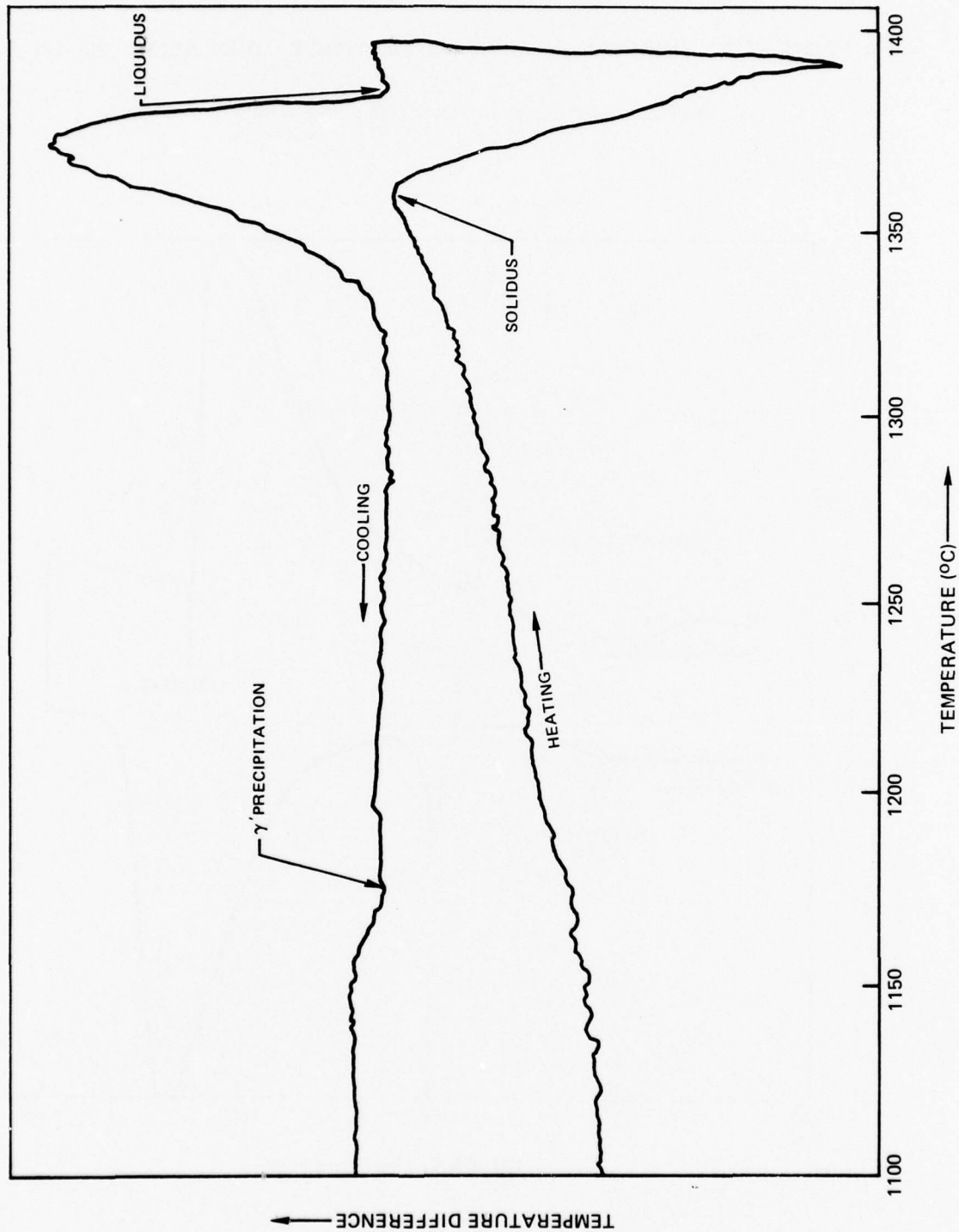

79–08–34–22

SCHEMATIC DRAWING OF DISK 1–8, SHOWING ORIENTATION OF CYLINDRICAL COORDINATES

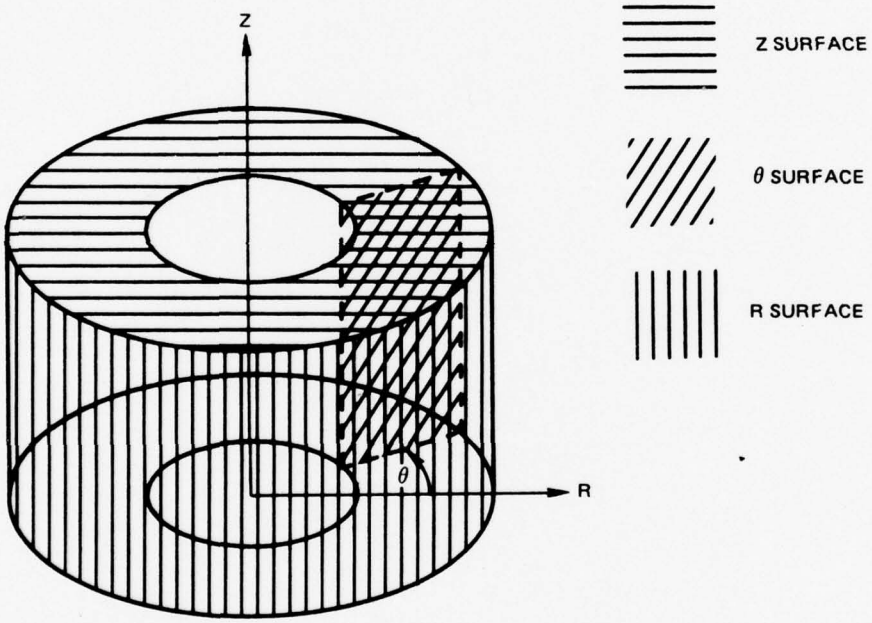

FIG. 36A

R FACE NEAR OUTER SURFACE, DISK 1–8, ALLOY 8–12–3

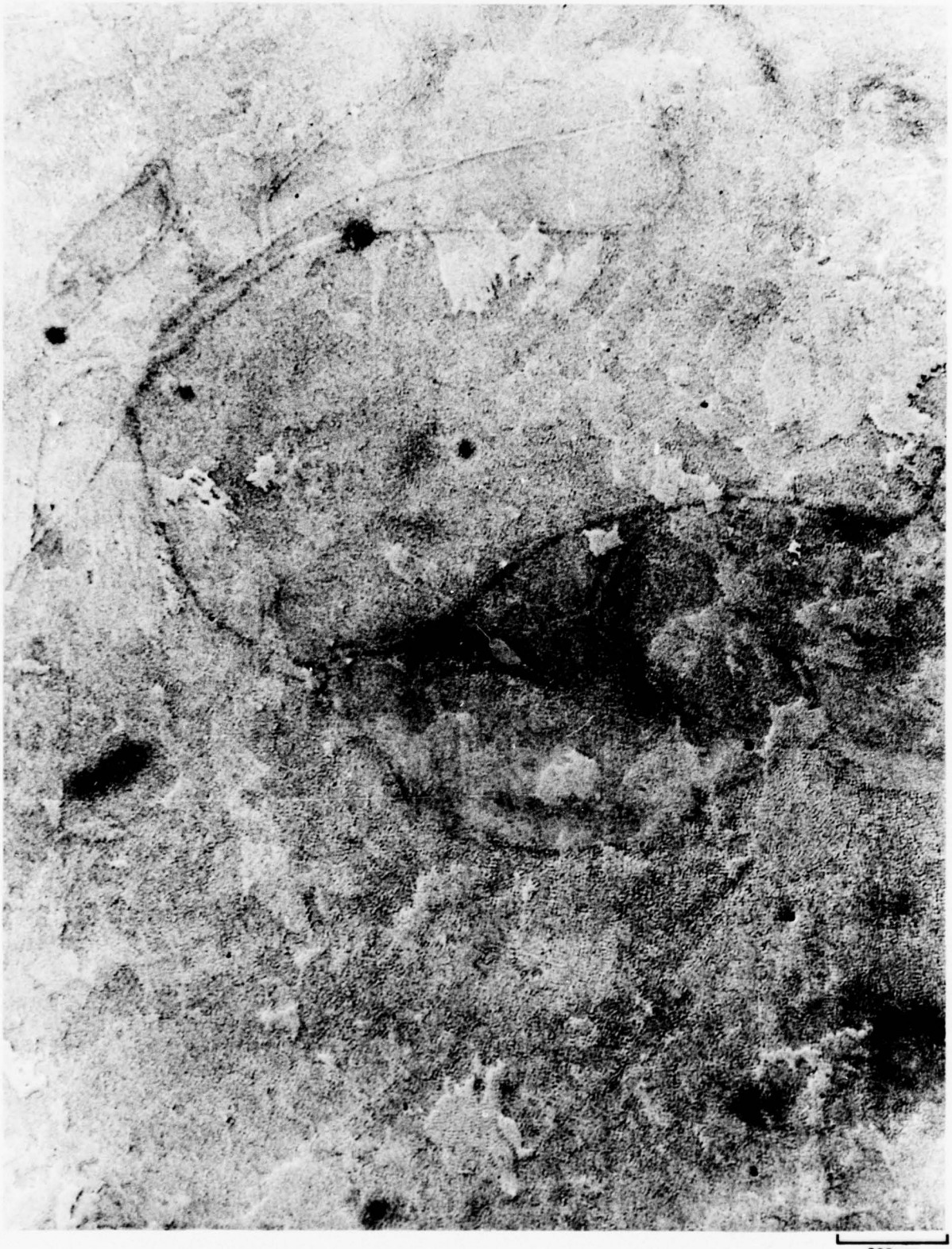

79–08–34–1

FIG. 36B

R FACE NEAR OUTER SURFACE, DISK 1–8, ALLOY 8–12–3

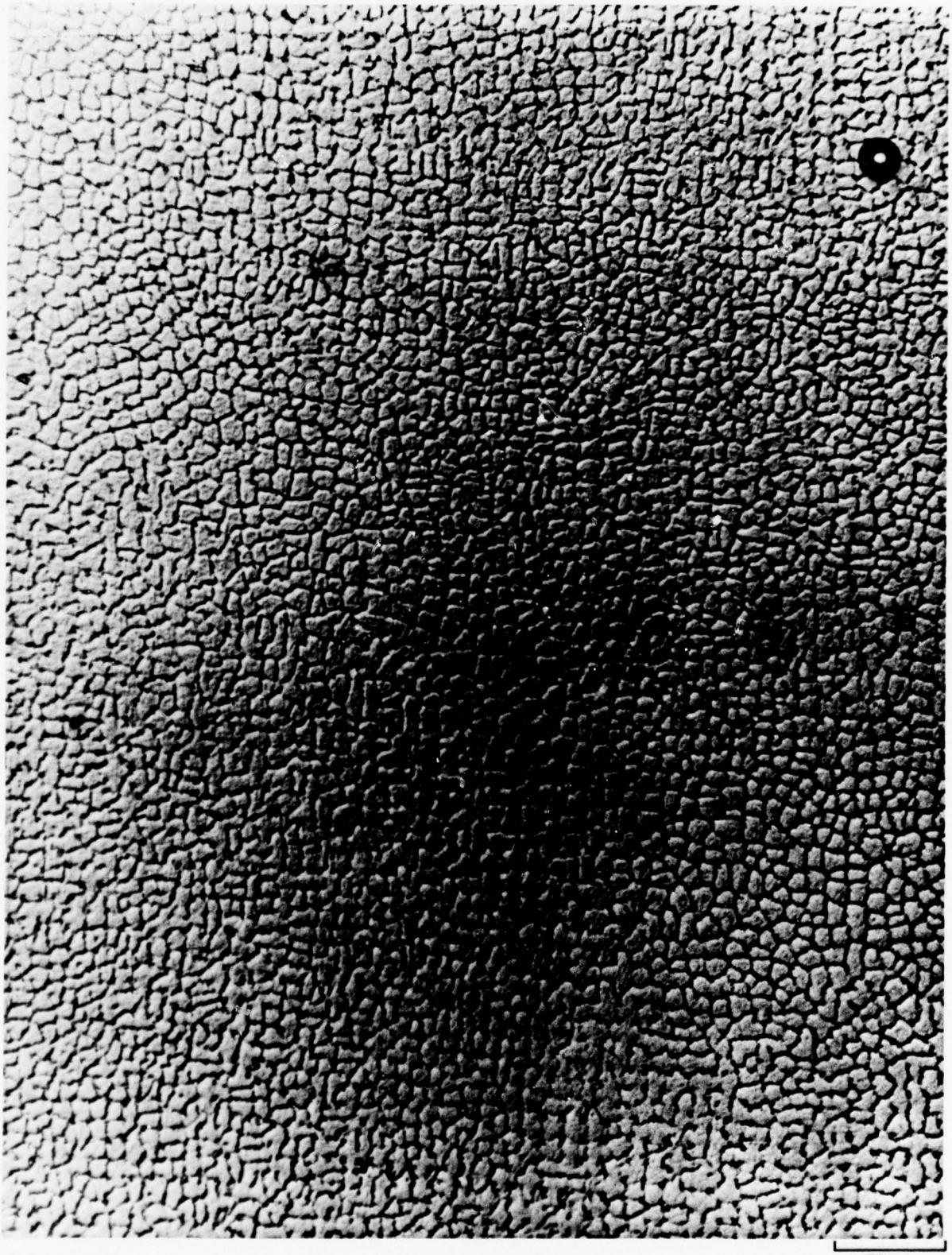

FIG. 37A

Z FACE NEAR STAINLESS STEEL SUBSTRATE, DISK 1-8, ALLOY 8-12-3

FIG. 37B

Z FACE NEAR STAINLESS STEEL SUBSTRATE, DISK 1–8, ALLOY 8–12–3

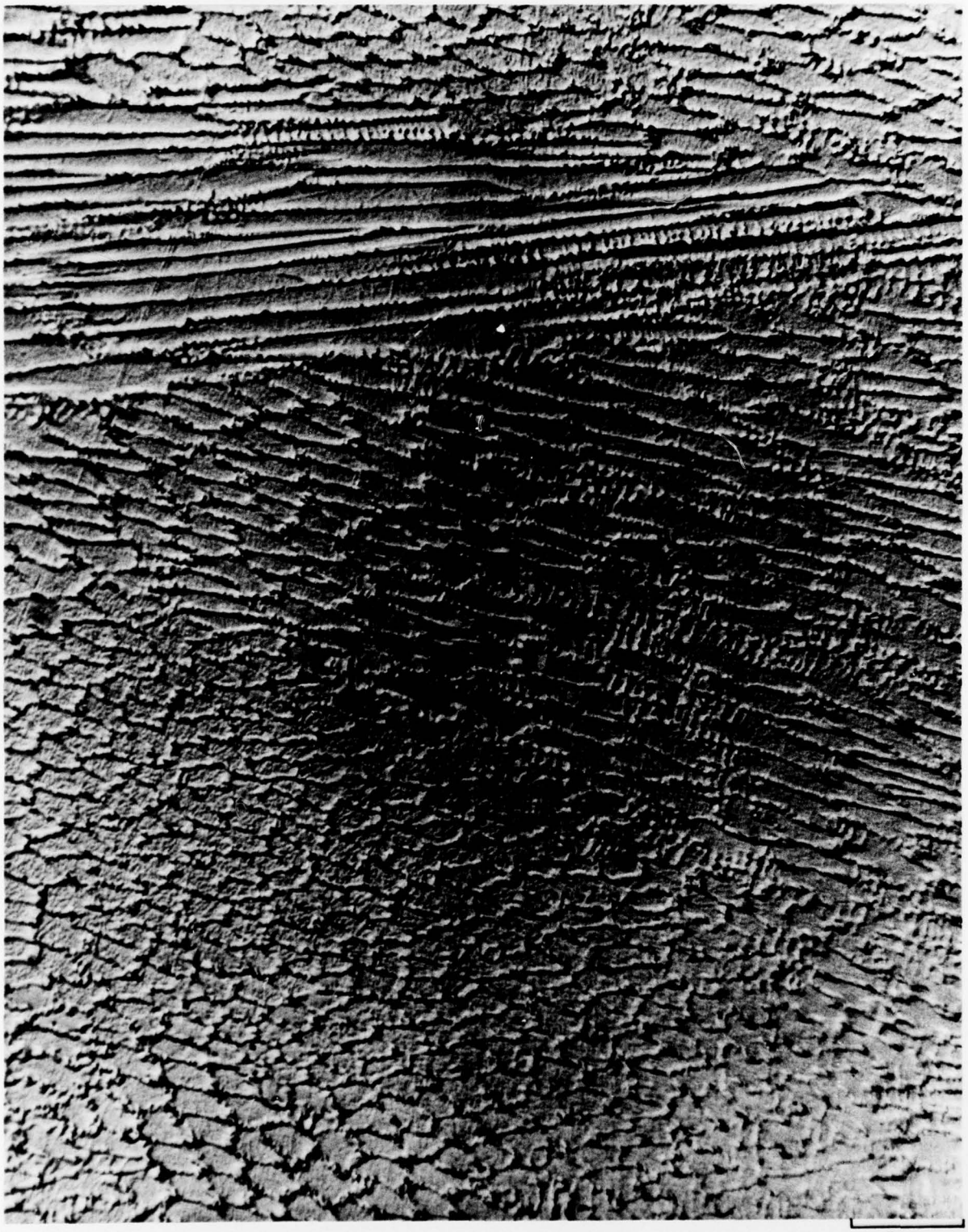

FIG. 38A

Z FACE NEAR MID–RADIUS, DISK 1–8, ALLOY 8–12–3

79–08–34–5

FIG. 38B

Z FACE NEAR MID–RADIUS, DISK 1–8, ALLOY 8–12–3

79–08–34–6

FIG. 39A

Z FACE NEAR OUTER SURFACE, DISK 1–8, ALLOY 8–12–3

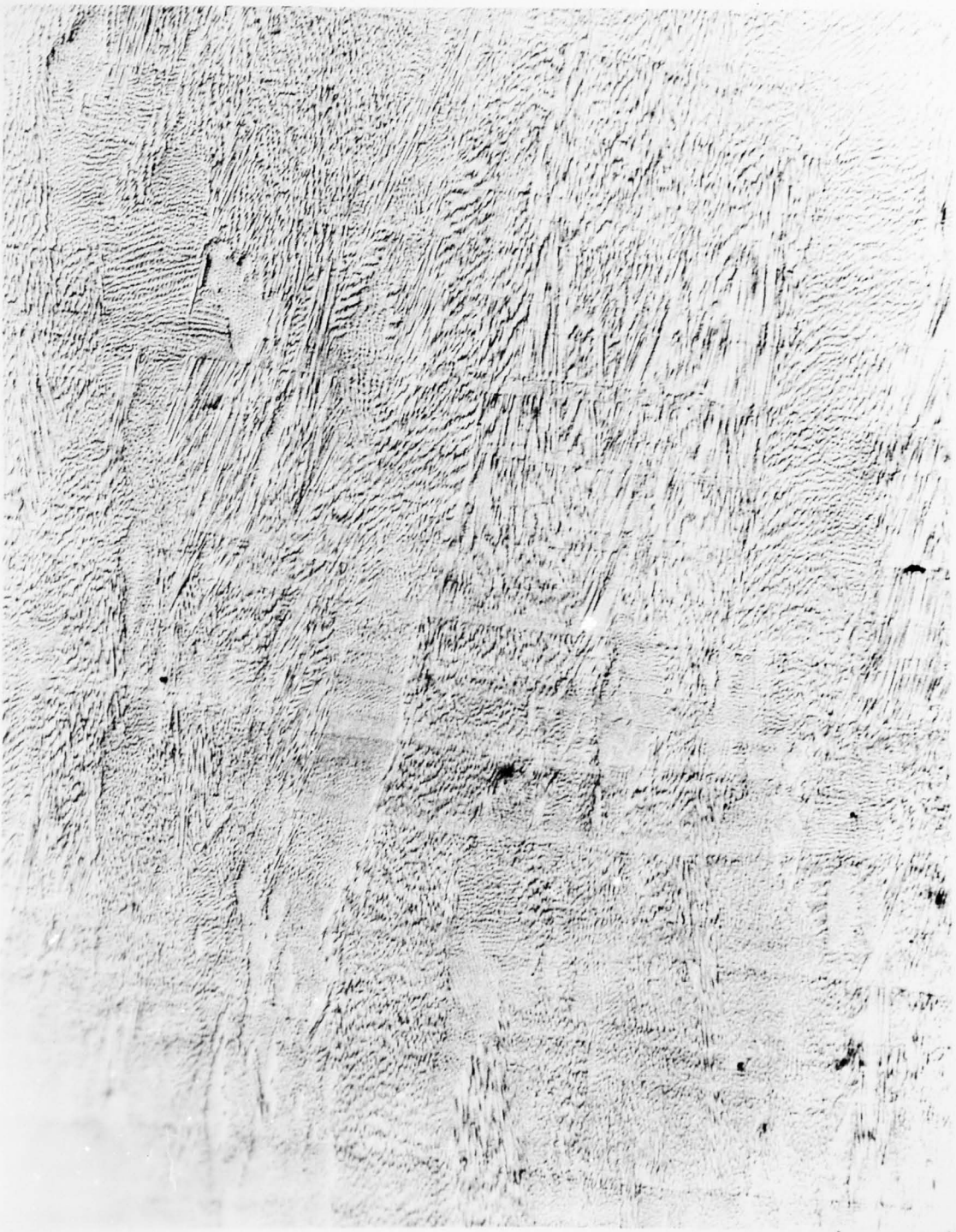

FIG. 39B

Z FACE NEAR OUTER SURFACE, DISK 1–8, ALLOY 8–12–3

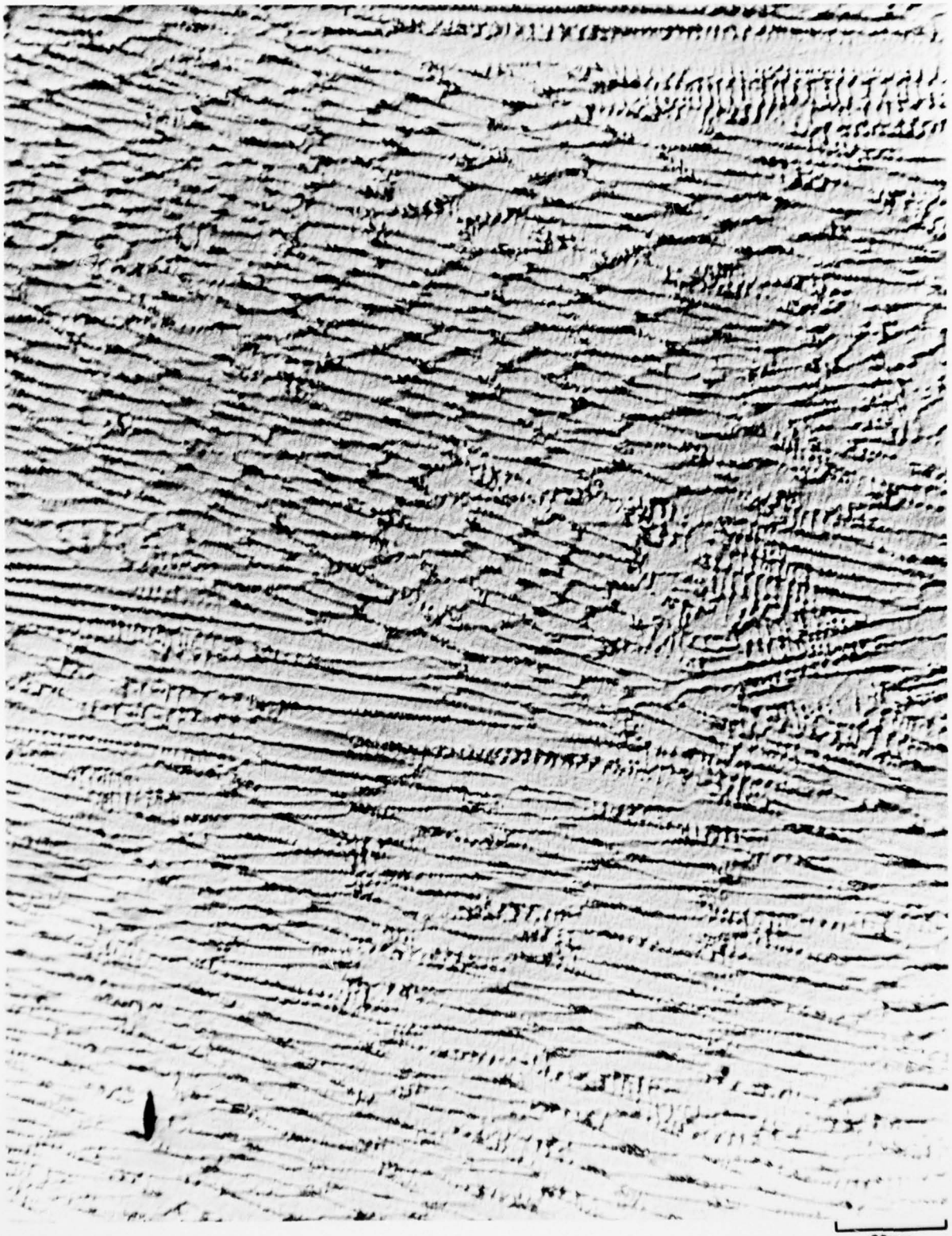

79–08–34–8

FIG. 40

θ FACE NEAR STAINLESS STEEL SUBSTRATE, DISK 1–8, ALLOY 8–12–3

79–08–34–9

FIG. 41

θ FACE NEAR OUTER SURFACE, DISK 1–8, ALLOY 8–12–3

79–08–34–10

TRANSMISSION ELECTRON MICROGRAPH OF R FACE, DISK 1–8, ALLOY 8–12–3

DENDRITIC GROWTH DIRECTION IS INCLINED TO THE FOIL NORMAL IN THIS REGION. EXAMPLES OF A POLYCRYSTALLINE INTERDENDRITIC PHASE ARE MARKED BY "A". SOME OF THE DENSE DISLOCATION TANGLES COMPRISING SUBBOUNDARIES ARE MARKED BY "B". NO GRAIN BOUNDARIES ARE PRESENT IN THE MATRIX IN THIS FIELD OF VIEW.

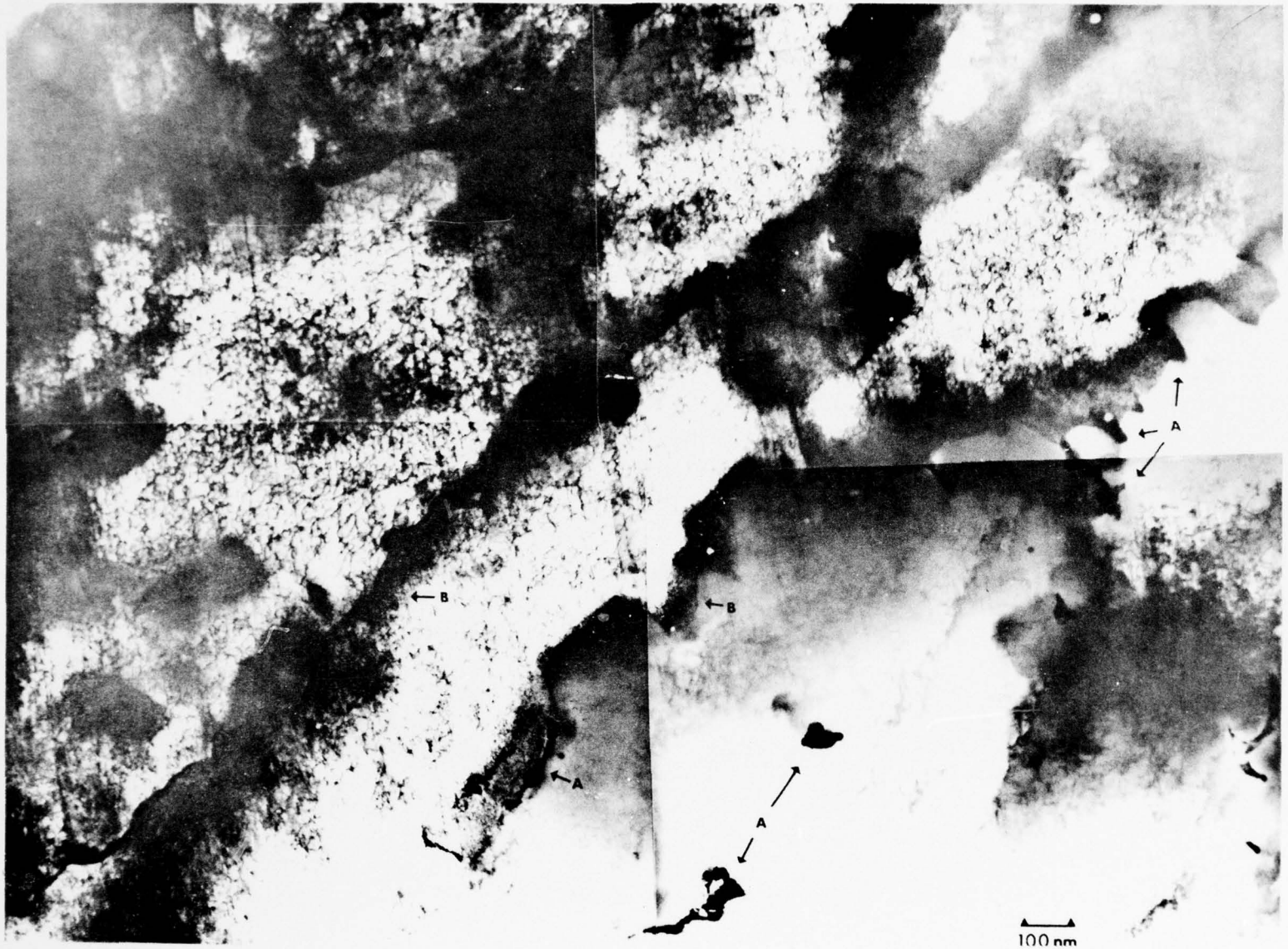

R79–914346–4

FIG. 42

79–08–34–24

FIG. 43

RADIOGRAPH OF 3.6 MM (0.14 IN) THICK PIECES SECTIONED FROM DISK 1–8

SEE FIGURE 25 FOR LIGHT MICROGRAPH

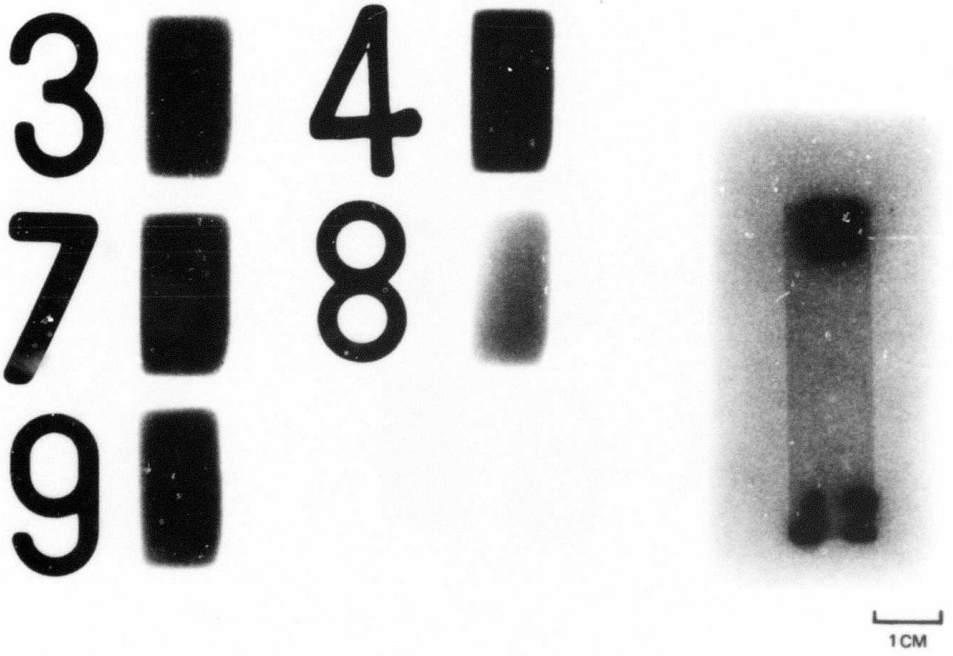

79–08–34–11

RADIOGRAPH OF 6.4 MM (0.25 IN) THICK PIECES SECTIONED FROM DISK 1–8

SEE FIGURE 25 FOR LIGHT MICROGRAPH

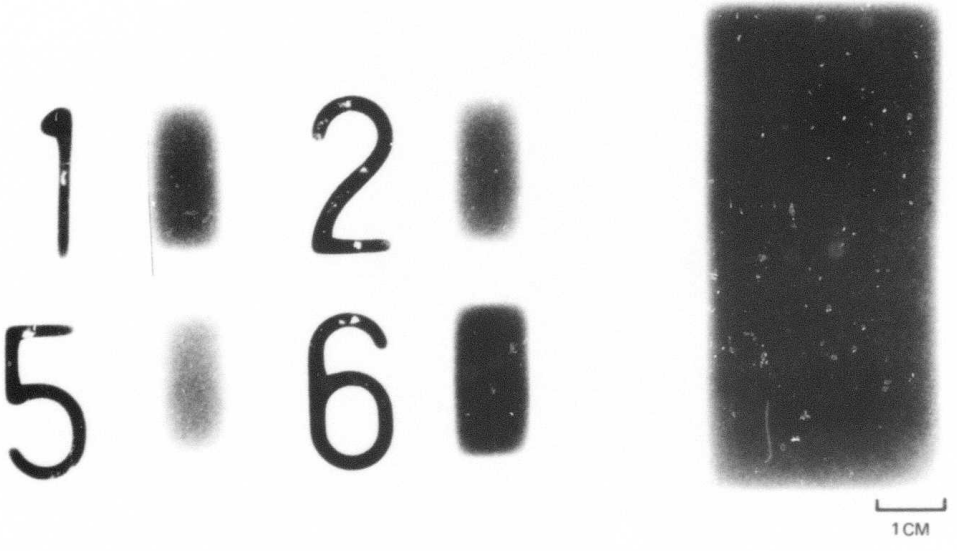

ENGINEERING STRESS–STRAIN CURVE OF TENSILE SPECIMEN FROM DISK 1–8

AMBIENT TEMPERATURE TEST. AXIAL SPECIMEN ORIENTATION (LOAD DIRECTION PARALLEL TO Z DIRECTION, THE DISK ROTATIONAL AXIS). YIELD STRENGTH AT 0.2% OFFSET: 1110 MPa (161 KSI). ULTIMATE TENSILE STRENGTH: 1352 MPa (196 KSI). ELONGATION: 12.8 %

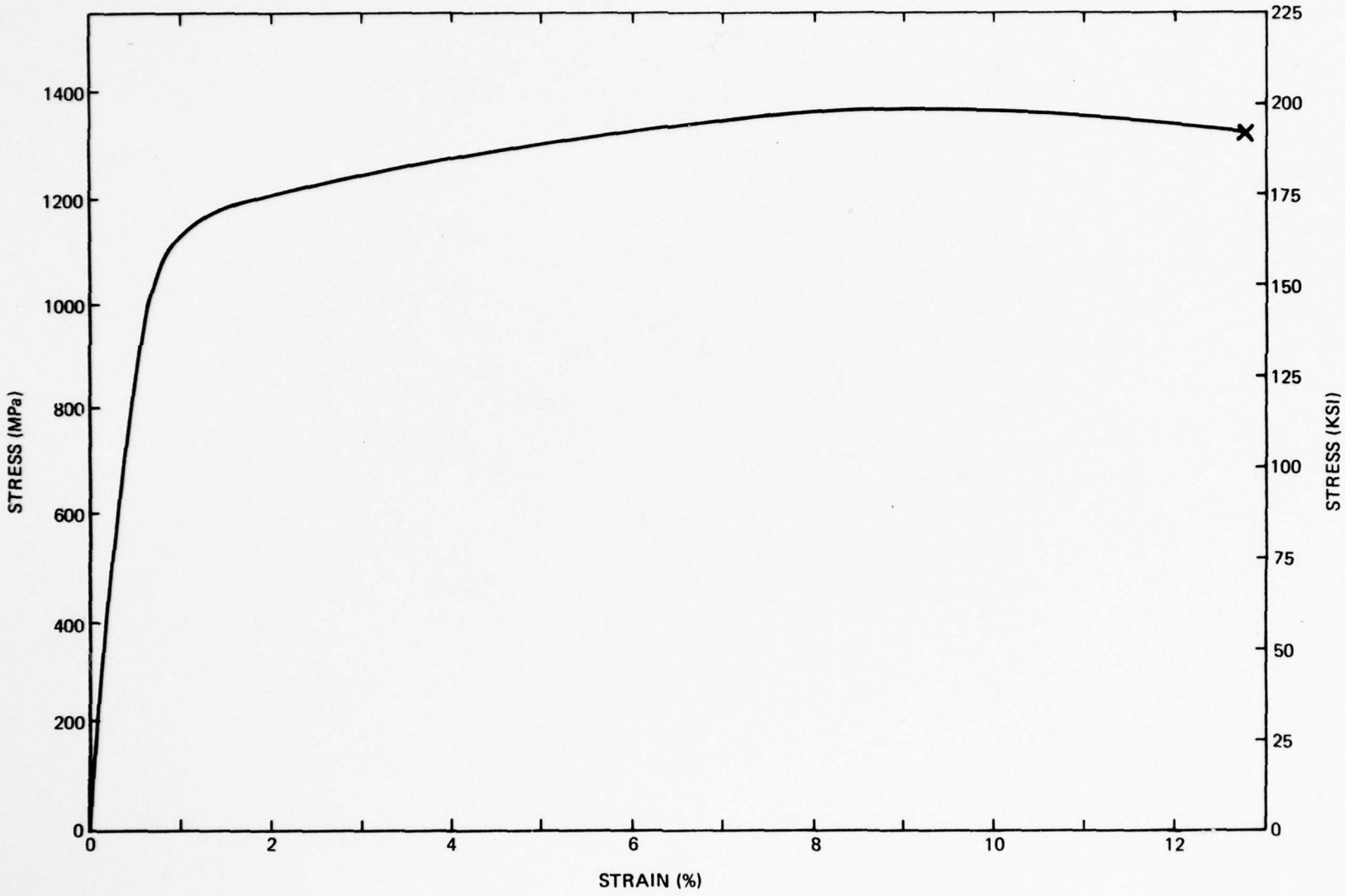

R79–914346–4

79–08–34–13

FIG. 45

APPENDIX A

SUMMARY OF STRESS ANALYSIS CALCULATIONS AND RESULTS
(Authored by Brice Cassenti of UTRC)

In order to analyze the stresses incurred in the buildup of a turbine disk, a two dimensional plane stress model was used. It can be shown that the thermal stress experienced by each deposited layer will be greater than the yield stress for the material, and therefore, each deposited layer will plastically yield. Consider the elastic deformation of a deposited layer. The thermal strain is given by

$$\varepsilon_{thermal} = \alpha \, \Delta T$$

for $$\alpha \sim 10 \times 10^{-6}/^{o}F \text{ and } \Delta T \sim -2000^{o}F$$

$$\varepsilon_{thermal} = -20 \times 10^{-3}$$

The Total strain can be written as

$$\varepsilon_{total} = \varepsilon_{thermal} + \varepsilon_{mechanical}$$

The relatively thin layer should be almost completely restrained by the bulk material below it and therefore

$$\varepsilon_{total} \approx 0$$

or $$\varepsilon_{mechanical} = -\varepsilon_{thermal} = 20 \times 10^{-3}$$

The stress can now be calculated from Hooke's Law as

$$\sigma = E \, \varepsilon_{mechanical} \text{ if } E \sim 20 \times 10^{6} \text{ psi}$$

Then, $\sigma \sim 400$ ksi, which is well above the yield stress for our materials.

As each layer is deposited on the mandrel, it goes into tension and yields plastically. However, as each subsequent layer is deposited it also goes into tension and thereby applies a compressional hoop stress to the layers beneath it. Plots of the ratio of hoop stress to yield stress versus distance from the center of the mandrel is shown in Figs. A-1 to A-7. Notice that the last layer to be deposited are always at the yield point ($\sigma\theta/\sigma_y = 1$) and that as more layers are added, the stress on the first layer progresses from a tensile yield point to a compressional yield point.

In order to calculate the radial stress and therefore the pressure exerted on the mandrel,and the melt, one assumes a differential element as in Fig. A-8.

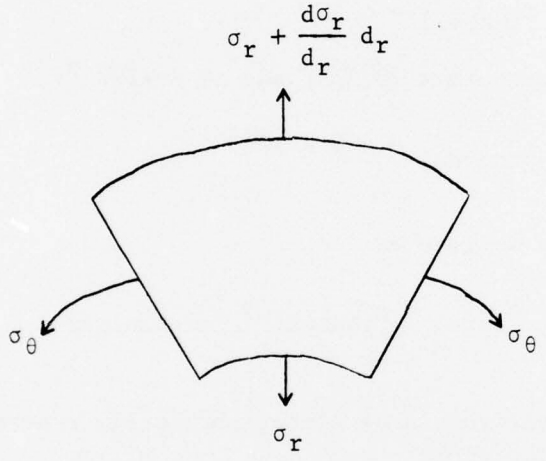

Fig. A-8

At equilibrium the following must be true: $(\sigma_r + \frac{d\sigma_r}{dr} d\,)(r+dr)d\theta - \sigma_r(rd\theta) - \sigma_\theta dr d\theta = 0$

or
$$\frac{d\sigma_r}{d_r} + \frac{\sigma_r - \sigma_\theta}{r} = 0 \qquad (1)$$

Assuming the Tresca yield condition holds at the outside layer

$$\sigma_r - \sigma_\theta = -\sigma_y \qquad (2)$$

Substitution of Eq. (2) into Eq. (1) yields

$$\frac{d\sigma_r}{d_r} = \frac{\sigma_y}{r} \quad \text{or} \quad \sigma_r = C_1 + \sigma_y \ln r$$

If the outside radius of the outermost layer is denoted as r_o, then the boundary condition that $\sigma_r = 0$ at $r = r_o$ may be imposed.

Therefore, $$\sigma_r = \sigma_y \ln(r/r_o).$$

It can clearly be seen that as the number of layers increases, the radial stress approaches the yield stress.

An additional analysis to provide a three dimensional model in which axial stresses may be incorporated has been performed. Using a MARC nonlinear finite element code and analyzing both elastic and plastic material response, a simulation of a deposit of a single layer upon a large mandrel was performed. The result was that high axial tensile stresses, of the order of one-half of the yield stress, were found below and to each side of the deposition. It appears that that after the LAYERGLAZE Process, most conventional superalloys crack because they do not have adequate strain capability to plastically yield to accommodate these high axial stresses. Several alloys developed in this program have shown adequate strain capability.